

# **Use of Thermal Stress Analysis for Defect Detection**

By

**Dhananjaya Kithsiri I.K.**

*Thesis  
Submitted to Flinders University  
for the degree of*

**Master of Engineering (Mechanical)**

College of Science and Engineering  
25.05.2023

---

# TABLE OF CONTENTS

<b>TABLE OF CONTENTS</b> .....	<b>I</b>
<b>ABSTRACT</b> .....	<b>III</b>
<b>DECLARATION</b> .....	<b>IV</b>
<b>ACKNOWLEDGEMENTS</b> .....	<b>V</b>
<b>LIST OF FIGURES</b> .....	<b>VI</b>
<b>LIST OF TABLES</b> .....	<b>VIII</b>
<b>1. INTRODUCTION</b> .....	<b>1</b>
1.1. Aim of the research .....	2
1.2. Scope of the research .....	3
1.3. Outline of the Research.....	3
<b>2. LITERATURE REVIEW</b> .....	<b>4</b>
2.1. Gaps in the field of research.....	7
<b>3. METHODOLOGY</b> .....	<b>8</b>
3.1. Theory related to Thermoelastic Effect.....	8
3.2. TSA Experiments .....	9
3.2.1. Preparation of specimens .....	10
3.2.2. Uniaxial (tensile) cyclic loading experiment.....	11
3.2.3. Flexural cyclic loading experiment .....	13
3.3. Finite Element Analysis .....	15
<b>4. RESULTS</b> .....	<b>17</b>
4.1. TSA experiments.....	17
4.1.1. Uniaxial (tensile) cyclic loading experiment.....	17
4.1.1.1. Effect of varying load amplitudes (Uniaxial).....	20
4.1.1.2. Effect of varying load frequencies (Uniaxial) .....	21
4.1.1.3. Effect of varying depths of damage (Uniaxial) .....	23
4.1.2. Flexural cyclic loading experiment .....	26
4.1.2.1. Effect of varying load amplitudes (Flexural).....	26
4.1.2.2. Effect of varying frequencies (Flexural) .....	27
4.2. FEA modelling .....	28
<b>5. DISCUSSION</b> .....	<b>30</b>
5.1. Varying load amplitudes (Uniaxial) .....	30
5.2. Varying frequencies (Uniaxial).....	34
5.3. Varying load amplitudes (Flexural) .....	35
5.4. Varying frequencies (Flexural).....	36
5.5. Varying depths of damages (Uniaxial).....	38
5.6. FEA models.....	39
<b>6. CONCLUSIONS</b> .....	<b>39</b>
<b>7. FUTURE WORK</b> .....	<b>40</b>

8. BIBLIOGRAPHY ..... 41

## **ABSTRACT**

This research evaluates the viability of Thermoelastic Stress Analysis (TSA) for detecting near surface internal defects in metal structural elements. The study explores the influence of varying loading conditions and defect locations on the detectability of damages using TSA. Experimental procedures were conducted under cyclical flexural and uniaxial loading, assessing the effects of load amplitude and frequency on damage detectability. A Finite Element model was also developed to evaluate its accuracy under different load conditions. The results demonstrate that TSA is highly effective in precisely detecting and locating internal defects, particularly at higher loading amplitudes and desired frequencies. Higher load amplitudes improve detectability, allowing for the identification of defects at greater depths from the surface. In-plane amplitude measurements excel at detecting surface-level damages, while quadrature amplitude measurements are more effective in identifying deeper internal damages. Higher frequency levels enhance TSA's capability to detect internal damages, although the relationship between frequency and TSA amplitude levels is nonlinear and requires further investigation. The flexural loading test encountered limitations, but statistical analysis suggests the effectiveness of TSA at higher flexural loading amplitudes. The Finite Element model accurately represents varying uniaxial loading cases but necessitates further study on the effects of load signal frequency. Overall, this research provides conclusive evidence supporting TSA as a highly capable full-field non-destructive testing method for detecting internal defects in metals. Future work should explore the nonlinear relationship between frequency and TSA amplitude levels and further investigate capabilities of TSA with flexural loading conditions.

# DECLARATION

I certify that this thesis:

1. does not incorporate without acknowledgment any material previously submitted for a degree or diploma in any university
2. and the research within will not be submitted for any other future degree or diploma without the permission of Flinders University; and
3. to the best of my knowledge and belief, does not contain any material previously published or written by another person except where due reference is made in the text.

Signature of student:

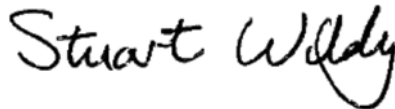


Print name of student: Dhananjaya Kithsiri Imiya Kankanamalage

Date: 25<sup>th</sup> May 2023

I certify that I have read this thesis. In my opinion it is/is not (please circle) fully adequate, in scope and in quality, as a thesis for the degree of Master of Engineering (mechanical). Furthermore, I confirm that I have provided feedback on this thesis and the student has implemented it minimally/partially/fully (please circle).

Signature of Principal Supervisor



Print name of Principal Supervisor: Dr Stuart Wildy

Date: 25<sup>th</sup> May 2023

# ACKNOWLEDGEMENTS

I am grateful to all those who have supported and guided me during the completion of this thesis. My sincere appreciation goes to my supervisor, Dr Stuart Wildy, for his invaluable guidance and encouragement. I am thankful for his expertise and constructive feedback that shaped this research work. I extend my gratitude to Dr John Codrington, Mr Aaron Baker and Mr Lloyd Gregory Button for their mentorship and support.

I would like to acknowledge the support of my colleagues and friends, whose camaraderie and discussions have contributed to my personal and professional growth. I am also grateful to my family for their love, belief in my abilities, and constant encouragement.

Lastly, I appreciate the work of authors, researchers, and scholars whose contributions have expanded the horizons of knowledge in this field. I am truly grateful for the involvement and belief of all those mentioned above in the successful completion of this thesis.

# LIST OF FIGURES

Figure 1 Phase lag between loading signal and thermal response & measurement points.....	9
Figure 2 An example 2D drawings of one of the specimen's dimensions and an image of the prepared specimen.....	10
Figure 3 Experimental setup of the uniaxial cyclic loading experiment .....	11
Figure 4 Focusing the IR camera with the help of a ruler.....	12
Figure 5 Experimental setup of flexural cyclic loading experiment.....	14
Figure 6 An image of the actual experimental setup of flexural loading experiment.....	14
Figure 7 Flow of FEA model in ANSYS Workbench 2020.....	16
Figure 8 Load signal at 15kN mean, 10kN amplitude and 6Hz. ....	17
Figure 9 Phase, In-plane and Quadrature images generated by microbolometer. ....	18
Figure 10 In-plane amplitude of TRS along a single line at the centre of the beam .....	19
Figure 11 Average in-plane amplitudes(X) over the width of the beam plotted along the length of the beam. ....	19
Figure 12 TRS in-plane amplitude(X) values at the centre of the beam for varying load signal amplitudes .....	20
Figure 13 Mean in-plane amplitude(X) over the width of the beam along the length of the beam for varying load amplitudes. ....	21
Figure 14 TRS in-plane amplitude(X) values at the centre of the beam for varying frequencies ....	22
Figure 15 Mean in-plane amplitudes(X) over the width of the beam for varying frequencies. ....	23
Figure 16 Mean TRS in-plane amplitudes(X) over the width of the beam for varying depths of defects.....	24
Figure 17 Calibrated mean TRS in-plane amplitudes(X) over the width of the beam for varying depths of defects. ....	25
Figure 18 Calibrated mean TRS in-plane amplitudes(X) over the width of the beam for varying depths of defects. ....	25
Figure 19 Mean TRS in-plane amplitude(X) over the width of the beam for varying loads.....	26
Figure 20 Mean TRS in-plane amplitude(X) over the width of the beam for varying frequencies. ...	27
Figure 21 Temperature variation (mK) visualized in the FEA model at 6Hz.....	28
Figure 22 In-plane temperature variation(mK) results of the FEA model for varying axial loads ....	29
Figure 23 In-plane temperature variation(mK) results of the FEA model for varying frequencies... 29	
Figure 24 Gaussian fitted curves of in-plane and quadrature amplitudes of the axial loading test at 10kN load amplitude, 15kN mean and 6Hz of frequency. ....	31
Figure 25 Mean values of the gaussian distributions against the load amplitudes. ....	32
Figure 26 Noise level against the peak levels.....	33
Figure 27 Mean values of the gaussian distributions against the frequencies. ....	34
Figure 28 Noise level against the peak levels.....	35
Figure 29 Mean values of the gaussian distributions against the displacement (loads) .....	36
Figure 30 Noise level against the peak levels.....	36
Figure 31 Mean values of the gaussian distributions against the frequencies. ....	37
Figure 32 Noise level against the peak levels.....	37
Figure 33 Noise level against the peak levels of in-plane amplitude(X) for varying depths .....	38

Figure 34 Noise level against the peak levels of quadrature amplitude(Y) for varying depths ..... 39



# LIST OF TABLES

Table 1 Test plan for uniaxial loading experiment.....	12
Table 2 Test plan for flexural loading experiment .....	15

# 1. INTRODUCTION

Non-destructive testing (NDT) involves the application of techniques that assess the structural soundness, surface defects, or metallurgical state of a material without causing any damage or affecting its ability to be used in its intended service (Dwivedi et al., 2018). NDT plays a vital role in ensuring the highest standards of product quality and the safe and reliable operation of components in various industries. It provides indispensable insights to designers and maintenance personnel by facilitating the identification and measurement of defects, stresses, and changes in the material's microstructure. By employing a range of non-invasive techniques, NDT allows for thorough assessment and evaluation without causing damage to the tested materials. This comprehensive approach to quality assurance and maintenance empowers stakeholders to make informed decisions, implement necessary repairs or modifications, and ensure the overall integrity and longevity of components in service. These findings are invaluable in making informed decisions regarding product design and maintenance schedules, ultimately ensuring the overall reliability and performance of the components (Raj, 2001).

Thermoelastic Stress Analysis (TSA) is an optical NDT method that enables the measurement of surface stresses on bodies through a non-contact, full-field approach. This technique utilizes the thermoelastic effect, whereby the application of cyclic loads to a material generates temperature variations. In adiabatic conditions, these temperature changes in isotropic materials are directly proportional to the sum of the two principal stresses on the material's surface (Gdoutos, 2022).

TSA offers several advantages over other NDT techniques depending on the application. One key advantage of TSA is its high sensitivity to surface stress concentrations, enabling the detection of stress gradients and variations across a structure. This capability proves particularly valuable in identifying stress concentrations around critical areas such as cracks, notches, welds, and joints, where failures are prone to occur. TSA also excels in providing a full-field analysis of stress distribution over a material or structure, capturing the spatial distribution of stress and visualizing stress patterns and concentrations in real-time. This feature distinguishes TSA from other NDT methods that rely on point-by-point measurements, enhancing the efficiency and accuracy of stress evaluation (Greene et al., 2008).

Real-time monitoring is another significant benefit offered by TSA. This capability allows for the continuous observation of stress changes over time, enabling the assessment of fatigue and failure mechanisms, especially in scenarios involving dynamic or cyclic loading conditions. The non-contact nature of TSA is advantageous for evaluating delicate or sensitive structures, as it eliminates the need for physical contact with the material being tested. This feature ensures that TSA does not introduce potential damage or alteration during the testing process, enhancing the integrity of the material under examination.

In terms of inspection speed, TSA offers relatively rapid evaluation and analysis compared to some alternative NDT techniques. The ability to measure and analyse stress distributions quickly proves advantageous for applications requiring efficient and timely evaluation. TSA also eliminates the need for extensive surface preparations in many cases. Unlike certain methods, TSA typically does not necessitate elaborate cleaning or coating of the material surface, saving valuable time and effort during the testing process. Moreover, TSA exhibits wide applicability, capable of being employed across a broad range of materials, including metals, composites, plastics, and ceramics. This versatility renders TSA suitable for various industries, such as aerospace, automotive, civil engineering, and manufacturing.

### **1.1. Aim of the research**

This research aims to evaluate the viability of using TSA technique for detecting near surface internal defects of a metal structural element and to evaluate the effects of varying loading conditions and defect locations on the detectability of the damages or defects in the structural member under consideration. To achieve this aim, following objectives were defined,

- Develop and carry out an experimental procedure to assess the effects of load amplitude and frequency of a steel beam under cyclical flexural loading on the detectability of the damages through TSA.
- Develop and carry out an experimental procedure to assess the effects of load amplitude and frequency of a steel beam under cyclical uniaxial loading on the detectability of the damages through TSA.
- Develop and carry out an experimental procedure to assess the effects of damage location relative to the observed surface of a steel beam under cyclical uniaxial loading on the detectability of the damages through TSA.
- Develop a Finite Element model for the cyclical uniaxial loading experiment and evaluate the accuracy of the model at for varying load amplitudes and frequencies.

- Critically analyse the data collected to evaluate the effect of each tested parameter on the detectability of damages through TSA.

## **1.2. Scope of the research**

There are numerous types of structural members that are made with various different materials depending on their applications. These structural members may undergo a range of loading scenarios during service including tensile, compressive, flexural, and combined loading cases and there are various types of defects or damages that could be found in these structural members. A number of NDT techniques are available for detecting these damages and monitoring the integrity of these members.

However, this research only focuses on studying the use of TSA method for detecting near surface damages in a steel beam while only cyclic uniaxial tensile loading and cyclic flexural loading cases are considered. The only type of defects studied in this research are holes or discontinuities and other types of defects are not investigated. When testing the detectability of the defects for varying parameters, only following parameters were investigated,

- load amplitude and frequency of a steel beam under cyclical flexural loading
- load amplitude and frequency of a steel beam under cyclical uniaxial loading
- damage location relative to the observed surface of a steel beam under cyclical uniaxial loading

## **1.3. Outline of the Research**

In order to achieve the goals and the overall aim of the research as mentioned in “1.1 Aim of the research” section, this thesis first reviews the literature relevant to TSA method to identify the gaps. Then the research methodology is established along with the theoretical aspects of the TSA method while specifying the equipment used and the test plan for each test in chapter 3 to ensure the repeatability of the study. In chapter 4, the results are presented in a functional manner with visual representations of thermal response data for better understanding of the reader. Chapter 5 critically analyses and discusses the results and finally chapter 6 and 7 provide the conclusions and suggestions for future work respectively.

## 2. LITERATURE REVIEW

All engineering structures are susceptible to degradation or damage due to environmental factors, mechanical influences, and natural aging processes. The integrity of an entire structure or its intended operation can be compromised by the damage to any individual component within it (Rucka, 2020). Therefore, industries such as aerospace, automotive, marine, power generation, and civil sectors consider it vital to detect damage and monitor structural health (Sause & Jasiūnienė, 2021).

To detect damage and monitor structural health, a variety of destructive and non-destructive testing (NDT) methods have been developed over time. NDT techniques offer advantages as they can identify both surface and internal damage in structural components without compromising their integrity (Mukhopadhyay & Mulaveesala, 2021). Compared to destructive testing, NDT methods are cost-effective, allow for repairs, and avoid the need for part replacement during inspections. Radiographic testing, vibration testing, eddy-current testing, acoustic emission testing, thermography, shearography, ultrasonic testing, and optical techniques are among the commonly used NDT methods. Another effective technique for damage detection is Thermoelastic Stress Analysis (TSA), which utilizes the thermoelastic effect to measure stress in beams (Takei et al., 2016).

### Thermoelastic Stress Analysis (TSA)

The TSA technique relies on the principle of thermoelastic effect, which involves the utilization of an infrared (IR) camera to detect minute temperature variations in a cyclically loaded structural member. By measuring these temperature changes, the stress within the member can be determined (Emery and Dulieu-Barton, 2010). The thermoelastic effect describes the interdependence between temperature and stress within a material. It states that alterations in temperature can induce dimensional changes in a material, leading to the development of stress. Conversely, the application of stress to a material can give rise to temperature variations. This phenomenon was initially elucidated by Lord Kelvin in 1853, highlighting the fundamental relationship between thermal and mechanical behaviour in materials (Wong et al., 1988). In adiabatic conditions, the temperature change in isotropic materials correlates directly with the sum of the two principal stresses acting on the surface (Gdutos, 2022).

To achieve accurate stress measurements, the cyclically loaded member needs to be excited at a frequency where a quasi-adiabatic state is reached. Loading signal data, obtained from displacement data or calculated displacement using an accelerometer, is necessary for precise stress level readings (Krstulovic-Opara et al., 2011).

The temperature differences observed through TSA are extremely small, typically around 0.001 °C. Although the theoretical foundation of the thermoelastic effect has been established for over 150 years, the practical application of TSA has emerged more recently, primarily driven by advancements in infrared (IR) detectors capable of accurately detecting minute temperature changes (Gdoutos, 2022). These techniques have proven effective in various applications, including evaluating design concepts, analysing fracture mechanics, detecting damage, monitoring fatigue, and analysing residual stress. Through its ability to analyse temperature fluctuations and their relationship to stress patterns, TSA has demonstrated its utility as a valuable tool in various fields of study and practical applications (Greene et al., 2008).

The SPATE (Stress Pattern Analysis by measurement of Thermal Emissions) system was the first commercially available thermoelastic stress analysis equipment. It used a CMT (Cooled Mercury Cadmium Telluride) infrared detector operating in the 8-12  $\mu\text{m}$  wavelength range and a motorized mirror system for point-by-point raster scanning of the test piece (Dulieu-Barton & Stanley, 1998).

A study by Ancona et al. (2016) have established the use of TSA in tracking crack propagation of fatigue cracks whereas a study conducted in 2017, Rajic and Brooks implemented a real-time crack tracking approach by integrating a TSA system with an X-Y movement stage. These approaches accurately determine the location of the crack tip, either by treating the coordinates as unknowns or by analysing the phase difference map between the loading signal and temperature response. However, they rely on assumptions of linear elastic fracture mechanics and require high-resolution data obtained under constant amplitude and frequency loading. Challenges arise when using low-cost sensors with limited resolution or when dealing with variable amplitude and frequency loading in industrial applications (Middleton et al., 2020). Researchers have explored the tracking of fatigue crack propagation using TSA, combining passive and active thermography methods, although these methods may be hindered by safety concerns (Hwang et al., 2019).

Another concept introduced involves tracking crack initiation and propagation using an optical flow-based method, which exhibits favourable performance with high-resolution TSA

data but may introduce errors when applied to lower resolution sensors or situations with variable loading conditions. Consequently, further investigation is warranted to comprehensively evaluate the effectiveness of TSA under diverse conditions and to determine its practical applicability in industrial settings (Middleton et al., 2020).

In a study by Kakei et al. (2016), the propagation of delamination damage in glass fiber reinforced composite materials was investigated using TSA. They used a woven Glass (0/90)/Epoxy composite sample with a deliberately created delamination and monitored the thermoelastic response using an infrared camera during step-cyclic loading with varying mean levels. Finite element analysis (FEA) with cohesive elements was performed to simulate delamination propagation under a monotonically increasing axial load. The TSA findings of the delamination crack length showed good agreement with microscopic analysis, and the measured crack growth rate reasonably matched the simulation results.

In another article by Rajic & Galea (2015), an experimental case study focused on monitoring an F/A-18 airframe structure during full-scale fatigue testing under loading conditions representative of flight spectra. This comprehensive study covers a significant duration, spanning nearly the lifetime of an aircraft. The case study provides evidence supporting the feasibility of the monitoring concept, demonstrating its effectiveness in assessing the structural integrity under realistic operational conditions. The paper highlights the potential of TSA as a valuable tool for SHM, enabling the detection and assessment of structural defects, damage, and performance degradation. Rajic discusses the underlying principles of TSA and its advantages in providing full-field stress analysis. The paper also discusses the integration of TSA with other SHM techniques, such as vibration monitoring and acoustic emission, to enhance the overall monitoring capabilities. Overall, the research emphasizes the promising prospects of combining TSA and SHM for effective structural health assessment and maintenance. However, the study also acknowledges certain limitations associated with the concept, shedding light on areas that require further attention and improvement.

Numerous other studies have explored the application of Thermoelastic Stress Analysis (TSA) in different areas of damage analysis. For instance, Emery and Dulieu-Barton (2010) conducted research on utilizing TSA for damage studies in glass reinforced polymer materials. Krstulovic-Opara et al. (2011) focused on evaluating impact damage in fibreglass

composite materials using TSA. Additionally, De Finis et al. (2020) explored the application of TSA in assessing stiffness degradation.

## **2.1. Gaps in the field of research**

Upon reviewing the available literature, the following gaps in research relevant to TSA technique was identified.

- No study has been carried out to evaluate the effectiveness of TSA technique for near surface internal damages of metals.
- No comprehensive research data available for effects of various loading conditions on the detectability of internal damages of metals using TSA method.
- No research data available for effects of depth of the defects' location relative to the surface observed with IR camera on the detectability of internal damages of metals using TSA method.



### 3. METHODOLOGY

This section investigates the theoretical concepts of thermoelastic stress analysis and discusses the experimental setup of this research that utilizes the TSA technique in depth. Important parameters under consideration for evaluating the effectiveness of using the TSA technique for internal damage detection will be discussed including the experimental setup for testing the effects of varying parameters on the detectability of the internal damages. Also, the specifications of the specimen being tested, and the equipment being used will be set to ensure the repeatability of the experiments. The two main experiments carried out for this research are as below,

1. Axial cyclic loading of a steel beam with internal defects at varying parameters
2. Flexural cyclic loading of a steel beam with internal defects at varying parameters

And finally, a Finite Element Analysis of the axial cyclic loading test of a steel beam with internal defects will be carried out at varying parameters and boundary condition using Ansys Workbench 2020 software.

#### 3.1. Theory related to Thermoelastic Effect

Equation (1) represents the basic correlation that describes the coupling between the principal stresses and the change in temperature which was discussed in introduction and literature review sections.

$$\delta T = -\frac{\alpha}{\rho C_p} T \delta \sigma \quad (1)$$

Where,

$\delta \sigma$  = change in scalar sum of the principal stresses (bulk stress),  $\delta T$  = temperature change yielded by  $\delta \sigma$ ,  $T$  = absolute temperature,  $\alpha$  = coefficient of thermal expansion,  $\rho$  = mass density,  $C_p$  = specific heat at constant pressure

$T$  is assumed to be constant since  $\delta T$  is at a scale of one thousandth the magnitude of  $T$  hence the relationship between  $\delta T$  and  $\delta \sigma$  is assumed to be linear.

### 3.2. TSA Experiments

The loading signal and the temperature variation curve may have a slight phase shift usually the temperature variation curve lagging the loading signal as shown in the Figure 1.

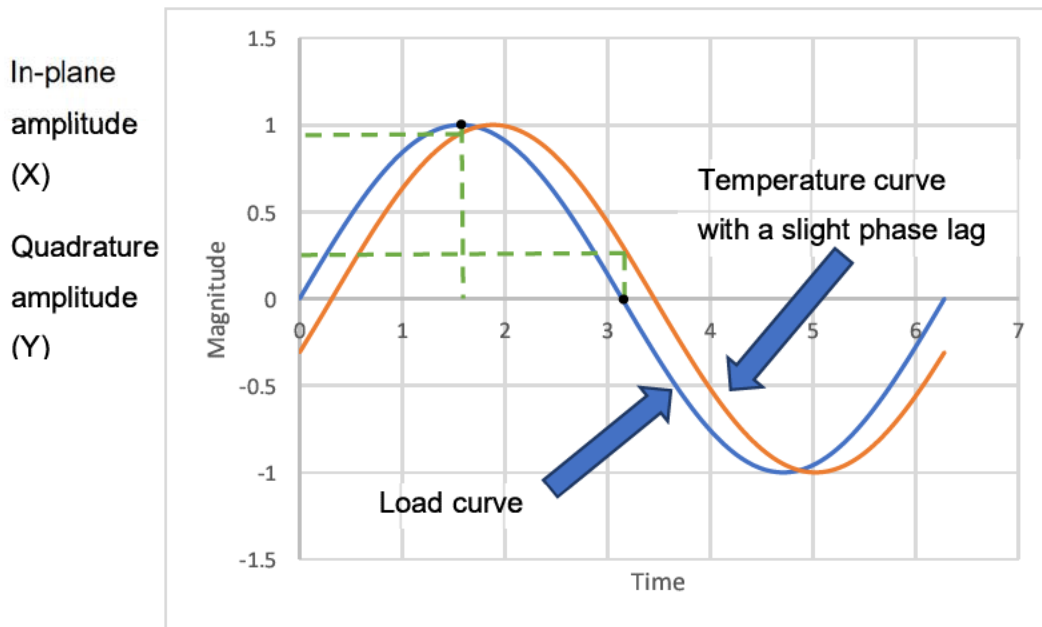


Figure 1 Phase lag between loading signal and thermal response & measurement points

Temperature measurements will be taken at two points. The in-plane amplitude of the temperature is the temperature amplitude measurement taken at the instant the load signal reaches its peak value, whereas the quadrature amplitude of the temperature is the temperature amplitude measurement taken at the instant the load signal reaches its mean value which is zero in the above example.

In-plane amplitude is proportional to the peak amplitude of the stress sum ( $\sigma_x + \sigma_y$ ) at a specific point on the structure. Whereas the quadrature reveals locations where heat diffusion is more significant, which occurs in locations of high-stress gradients, such as cracks or small defects. (Rajic & Galea, 2015)

### 3.2.1. Preparation of specimens

Four mild steel beams were prepared that are 600mm long, 25mm wide and 6mm thick. Each of them had 18 holes drilled from the side of the beam through the width to simulate damages or defects with 25mm gaps in between. Each hole was 1mm in diameter. Each beam has 75mm long solid clamping zone with no holes being present. First beam's holes were located 1mm below the surface of observation of the beam or at 1mm depth while the other three beams had holes located 1.5mm, 2.5mm and 3mm (at the centre) below the surface. These depth measurements were measured from the surface to the centre of the holes. The beam with holes at 1.5mm depth is shown in the Figure 2 as an example.

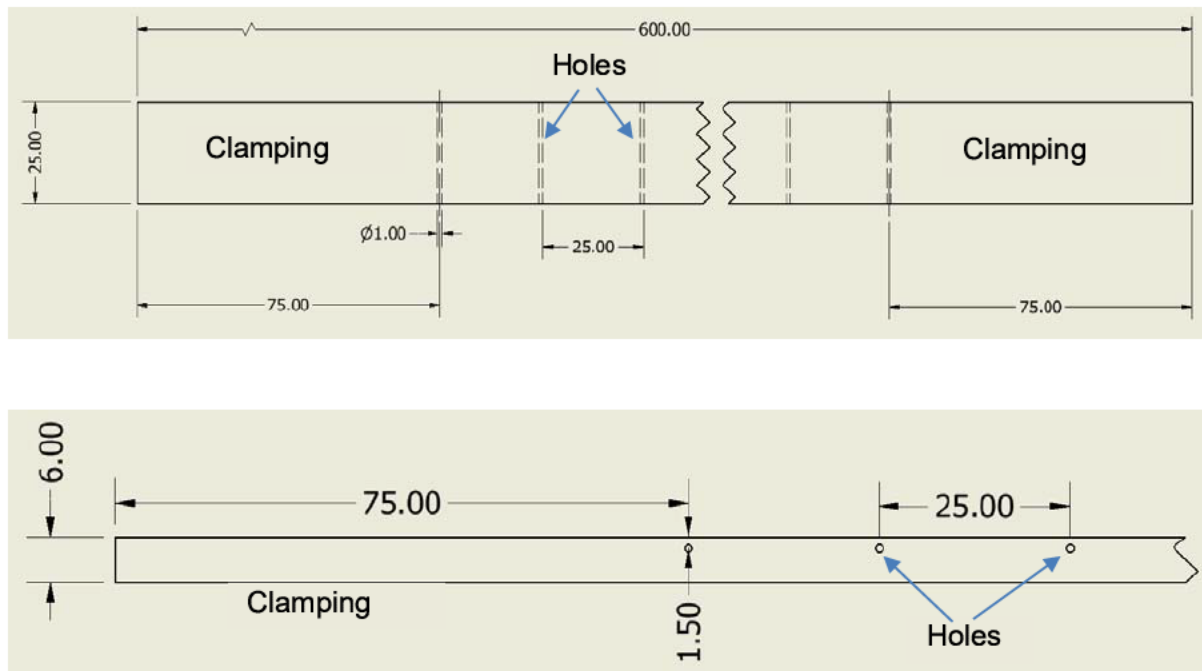


Figure 2 An example 2D drawings of one of the specimen's dimensions and an image of the prepared specimen

These four specimens were spray painted using a non-reflective paint (Appendix A) in order to avoid any thermal reflections when the experiment is being carried out.

### 3.2.2. Uniaxial (tensile) cyclic loading experiment

For this experiment, an Instron machine was used in order to apply a cyclic axial load to the specimens, a microbolometer was used to measure temperature variations, and finally a Data Acquisition system (DAQ: SIRGTESTEQ-003) and a computer with MiTE software was used for acquiring and recording data from the microbolometer. Figure 3 shows the experimental setup for this experiment.

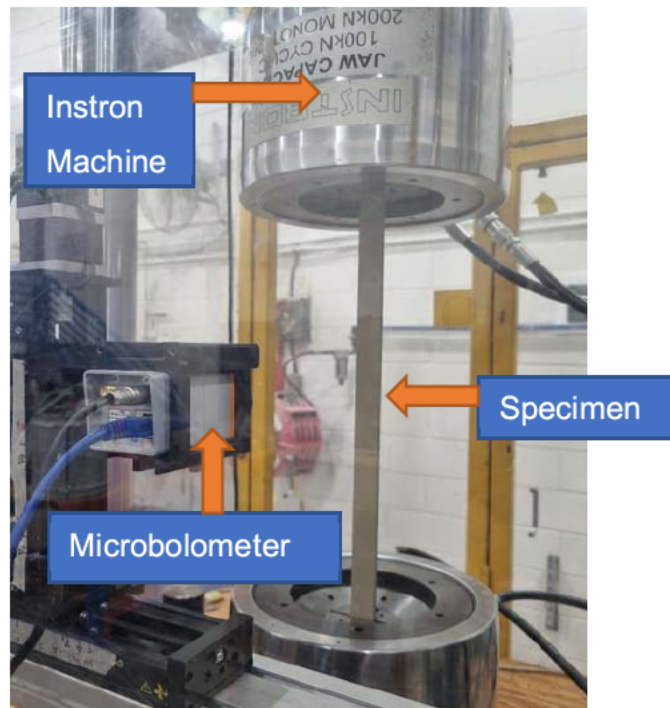


Figure 3 Experimental setup of the uniaxial cyclic loading experiment

Before starting the experiment, it was important to make sure that the microbolometer was focused on the surface of the specimen to be observed. This was achieved by attaching a thin metal ruler using a magnet to the specimen surface and then manually adjusting the focus ring of the microbolometer until it captured a sharp image of the numbers on the ruler as shown in Figure 4.

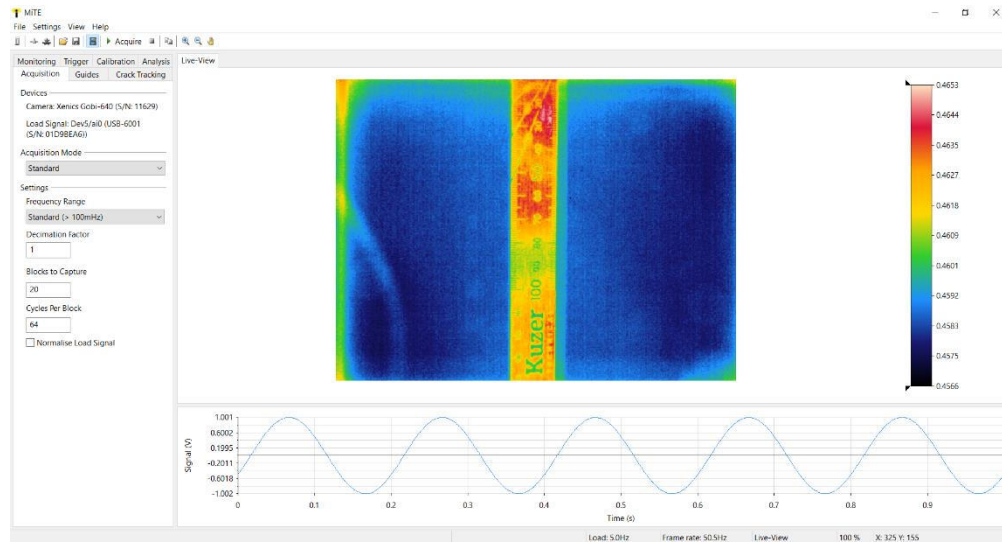


Figure 4 Focusing the IR camera with the help of a ruler.

In order to evaluate the effects of different parameters on the detectability of the damages or holes in the beam, tests were carried out at varying load amplitudes, varying frequencies and varying hole depths. Following Table 2 represents the tests carried out for axial cyclic loading case,

Study	Sample	Frequency (Hz)	Load (kN)
Load	Hole depth of 1 mm	6 Hz	Signal – Sinusoidal  - Mean = 15 kN  - Amplitudes (tensile) = 2, 4, 6, 8, 10 kN
Frequency	Hole depth of 1 mm	2 Hz, 4 Hz, 6 Hz, 8 Hz, 10 Hz	Signal – Sinusoidal  - Mean = 15 kN  - Amplitude (tensile) = 10 kN
Depth	Hole depths of 1 mm, 1.5 mm, 2.5 mm, 3 mm, 3.5 mm, 4.5 mm, and 5 mm.	Best frequency (6 Hz)	Signal – Sinusoidal  - Mean = 15 kN  - Amplitude (tensile) = 10 kN

Table 1 Test plan for uniaxial loading experiment

The 3.5mm, 4.5mm and 5mm hole depths were achieved simply by flipping over the 2.5mm, 1.5mm and 1mm beams respectively to observe the temperature variations of the opposite surface using the microbolometer.

### **3.2.3. Flexural cyclic loading experiment**

For this experiment only the beam with holes at 1mm depth was utilized which was fixed on one end using a metal clamp to simulate a cantilever beam arrangement. In order to apply a flexural cyclic load to the specimen 10mm below the free end, an Electromagnetic Shaker (EMS) was utilized, and a signal generator (Agilent 33120A) was used for determining the load signal. The signal generated by the signal generator was fed through an oscilloscope (Agilent 54622D) and a signal amplifier (LDS PA25E) to increase the amplitude of the signal which was then fed into the EMS.

The actual displacement cycle of the beam was then captured using a Laser Displacement Sensor (LDS) at 100mm below the free end of the beam and this signal was fed to a computer with MiTE software through a Data Acquisition system (DAQ: SIRGTESTEQ-003). The microbolometer was mounted on a tripod and the same technique of focusing the sensor on the surface of the beam which was used in axial loading experiment was utilized to obtain a sharp image. Temperature measurements were recorded at the fixed end of the beam as it undergoes the highest stresses and the lowest displacements. The experimental setup for this experiment is illustrated by the Figure 5.

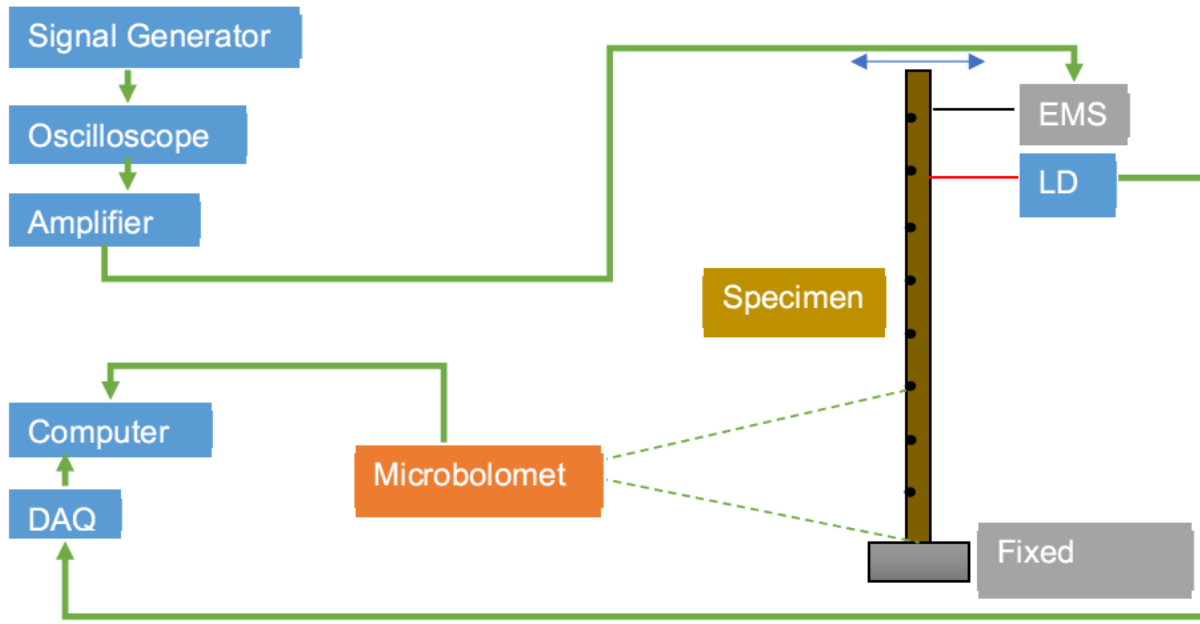


Figure 5 Experimental setup of flexural cyclic loading experiment

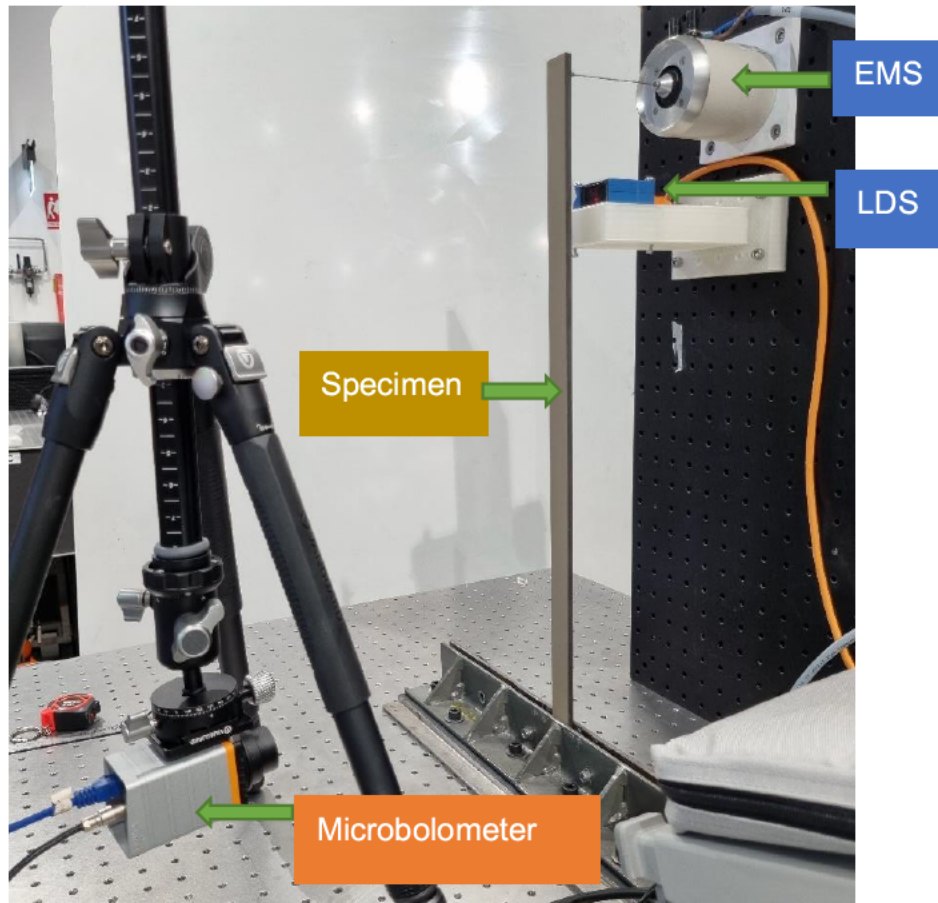


Figure 6 An image of the actual experimental setup of flexural loading experiment

In order to evaluate the effects of different parameters on the detectability of the damages or holes in the beam, tests were carried out at varying load amplitudes and varying frequencies. Table 1 represents the tests carried out for flexural cyclic loading case,

<b>Study</b>	<b>Sample</b>	<b>Frequency (Hz)</b>	<b>Displacement (Measured by LDS)</b>
Displacement	Hole depth of 1 mm	5 Hz	Signal – Sinusoidal  - Mean = 0  - Displacement Amplitudes (from neutral position) = 0.5mm, 1.5mm, 1mm, 2mm
Frequency	Hole depth of 1 mm	1 Hz, 2.5 Hz, 5 Hz, 7.5 Hz, 10 Hz	Signal – Sinusoidal  - Mean = 0  - Displacement Amplitude (from neutral position) = 2mm

Table 2 Test plan for flexural loading experiment

### **3.3. Finite Element Analysis**

Ansys Workbench 2020 was used for Finite Element Analysis (FEA) of the axial loading case of the specimens. The exact dimensions of the actual specimens used in the axial cyclic loading test were used for creating 2D model of the beams except for the shape of the holes. Even though the actual specimens contain holes that have circular cross sections with 1mm diameter, the 2D model of the specimen was created with holes that have 1mm x 1mm square shaped cross sections. The reason for this was to reduce the complexity of the mesh used for the FEA. The effect of this was assumed to be negligible as the main goal of this experiment was to determine how distinctively the holes can be separated from the temperature variation data collected from the FEA and to compare it with the data from the



real-world tests. Boundary conditions were applied to simulate the two axial loading tests with the varying loads and the varying frequencies. Finally, the test with varying depth of holes were simulated by carrying out the analysis on separate 2D models with holes at varying depths similar to the axial loading test. Figure 7 illustrates the flow of the FEA model developed.

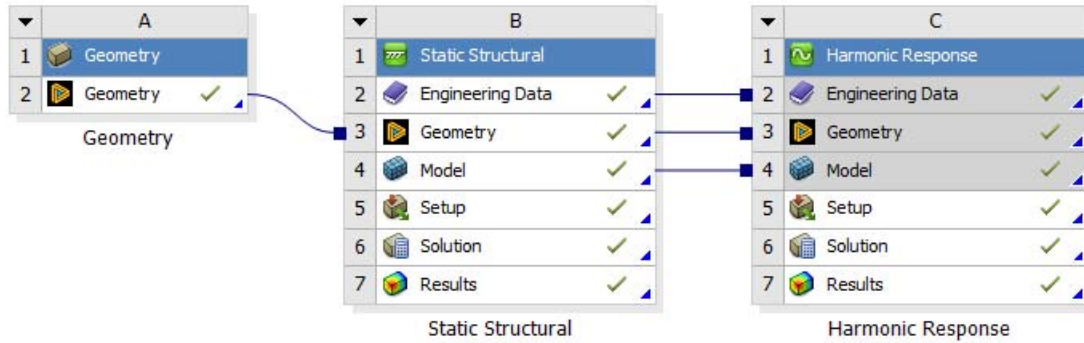


Figure 7 Flow of FEA model in ANSYS Workbench 2020

Equation (2) which is another form of equation (1) that describes thermoelastic theory, explained by Sathon & Dulieu-Barton (2005), was utilized in the FEA model in order to convert the Structural FEA model results into the Thermal response.

$$k\nabla^2 T - \rho \cdot c_p \frac{\partial T}{\partial t} = T_0 \alpha \frac{\partial \sigma_1}{\partial t} \quad (2)$$

Where,

$k$  = thermal conductivity,  $\rho$  = material density,  $T_0$  = absolute temperature,  $T$  = temperature field,  $c_p$  = specific heat at constant pressure,  $\sigma_1$  = first stress invariant,  $\alpha$  = coefficient of thermal expansion

## 4. RESULTS

### 4.1. TSA experiments

Temperature data during the axial cyclic loading tests were recorded using MiTE software as mentioned in the methodology section where the load signal was also fed to the computer as a reference signal in order to identify the phase lag between the load signal and the thermal response curve. However, the thermal response data recorded from the microbolometer through MiTE software does not illustrate actual temperature variation values, instead the data recorded represents a proportional correlation to the temperature variations due to the thermoelastic effect which will be referred to as the Thermoelastic Response Signal or TRS in this thesis. In other words, the amplitude (A) of TRS at any given point correlates proportionally to the temperature variation due to the thermoelastic effect at that point, which ultimately correlates to the stresses in the beam.

#### 4.1.1. Uniaxial (tensile) cyclic loading experiment

Figure 9 shows an example of the images of in-plane amplitude(X), quadrature amplitude(Y) and phase angle ( $\phi$ ) recorded by MiTE software using the data from microbolometer during the axial cyclic loading tests at 15kN mean tensile load, 10kN load signal amplitude and 6Hz frequency of the beam with holes at 1mm depth.

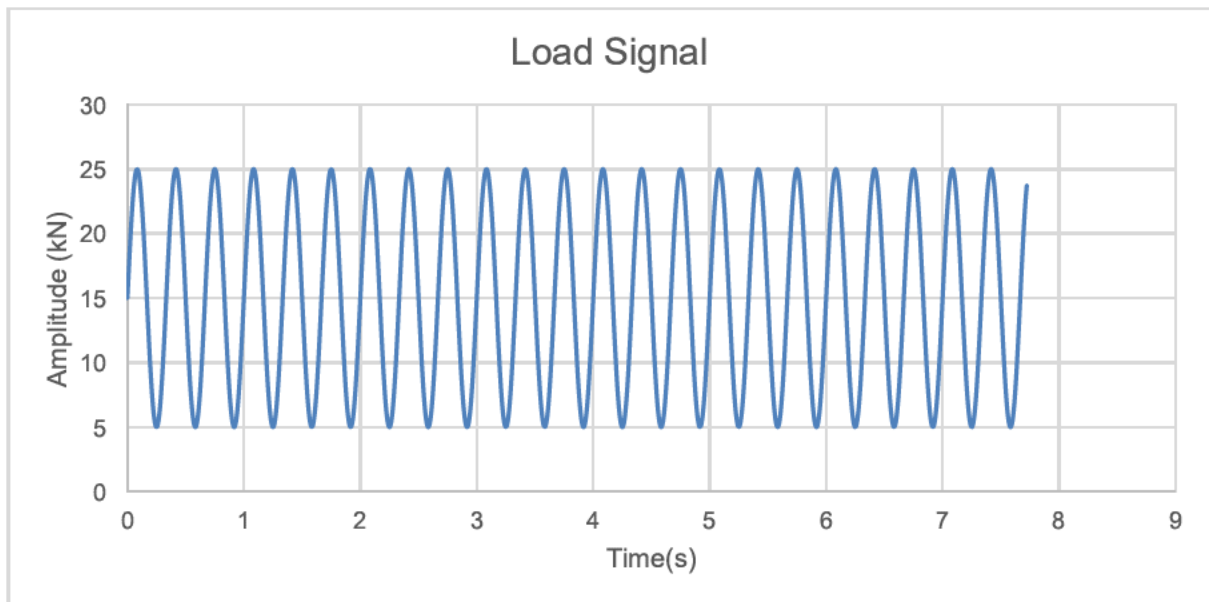


Figure 8 Load signal at 15kN mean, 10kN amplitude and 6Hz.

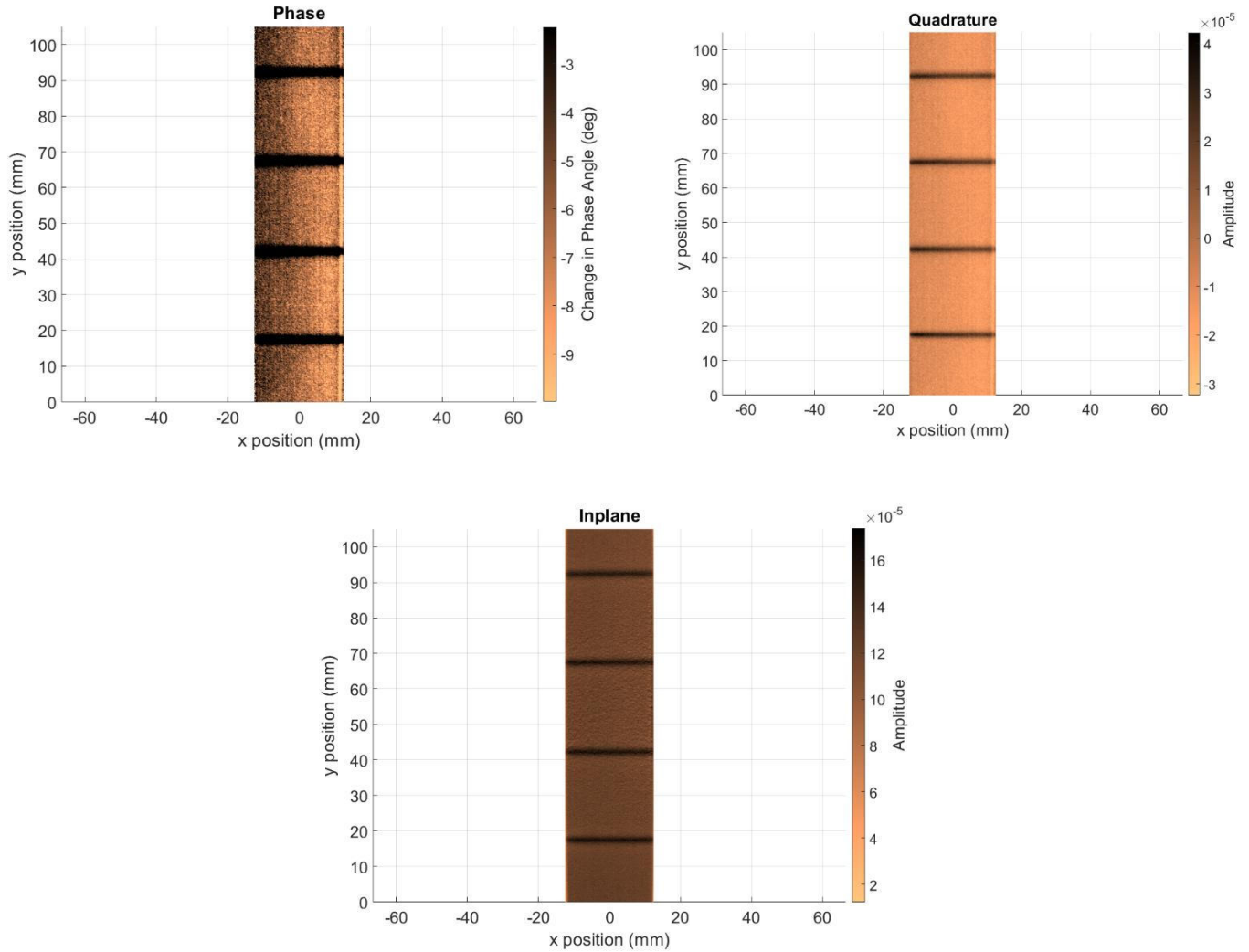


Figure 9 Phase, In-plane and Quadrature images generated by microbolometer.

Both the in-plane and quadrature images are quite promising as they both clearly show a higher amplitude of the thermoelastic response signal at the locations of the holes indicated by the clear and distinct darker lines in the images. Meanwhile the phase angle image indicates that there is minimum phase lag which is less than  $-3^\circ$  of phase angle at the locations of holes and a slightly higher phase angle at the undamaged areas.

A MATLAB script was developed to process these images. First, the TRS in-plane amplitude(X) values at the centre of the beam were plotted against the position along the length of the beam as illustrated in the Figure 10.

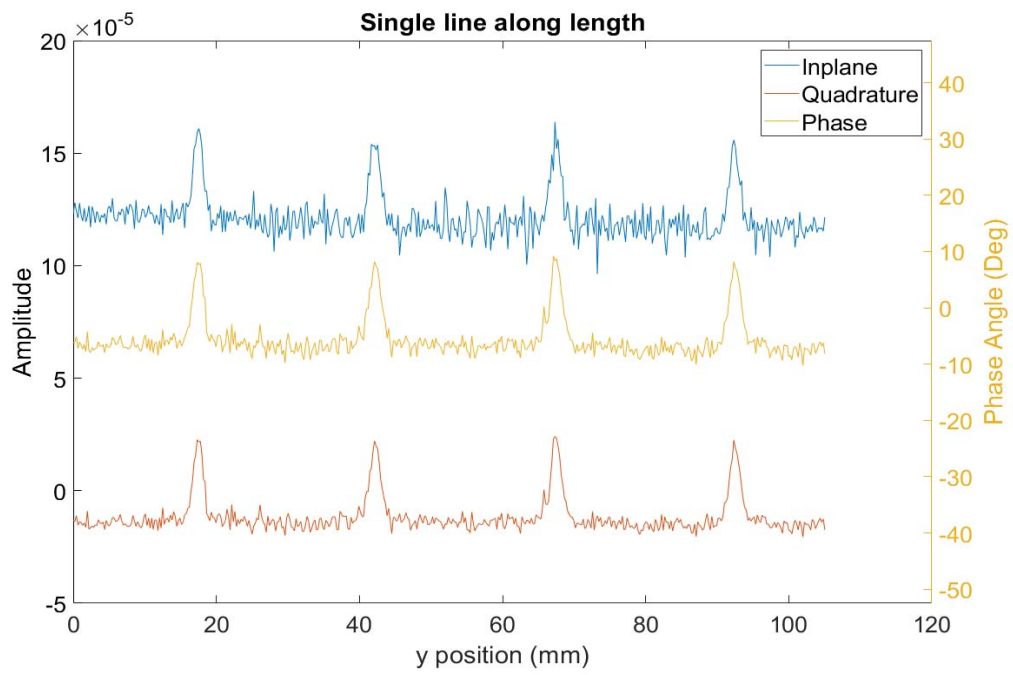


Figure 10 In-plane amplitude of TRS along a single line at the centre of the beam

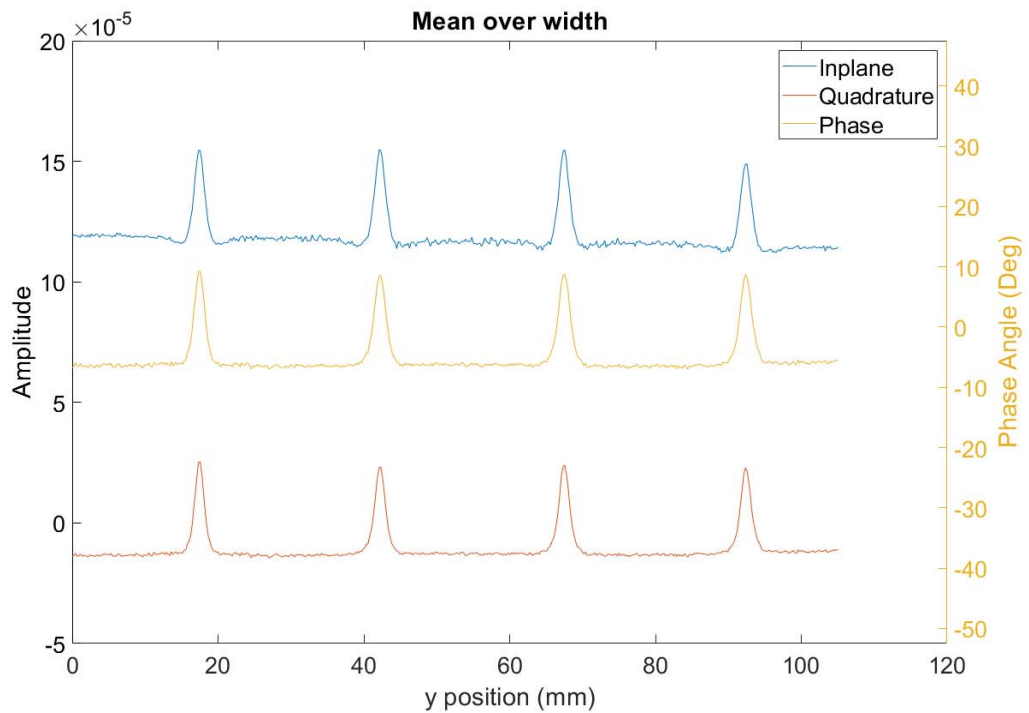


Figure 11 Average in-plane amplitudes(X) over the width of the beam plotted along the length of the beam.

This graphs in Figure 10 illustrates clear peaks of in-plane and quadrature amplitude values at the locations of the holes. Even though there is some noise present, the peaks are clearly

distinguishable from the noise upon visual inspection of the plot. However, the noise in these plots can be further reduced by calculating the mean in-plane amplitudes(X) over the width of the beam along the length of the beam. Figure 11 shows a plot of these mean amplitudes plotted against the location along the length of the beam which illustrates that the noise levels are reduced after taking the mean in-plane amplitudes(X) over the width of the beam. Peaks with very similar heights above the base amplitudes are present at each location of holes in observed area of the beam and they are clearly distinctive in both in-plane and quadrature graphs while the phase difference between load signal and thermoelastic response is between  $\pm 10^\circ$ .

#### 4.1.1.1. Effect of varying load amplitudes (Uniaxial)

In order to observe the effect of varying amplitudes of the load signal on the TRS recorded by the microbolometer, the same specimen was tested at 2kN, 4kN, 6kN, 8kN, and 10kN load amplitudes as specified in the methodology section. Figure 12 shows the TRS in-plane amplitude(X) values at the centre of the beam plotted against the position along the length of the beam for each of the load amplitude in the same graph.

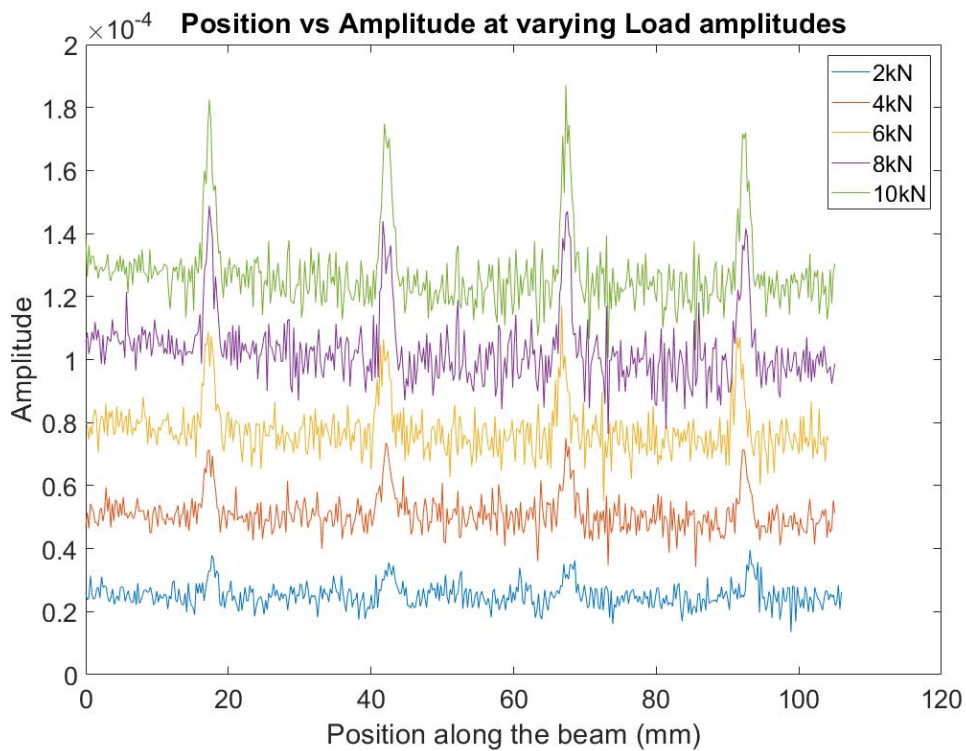


Figure 12 TRS in-plane amplitude(X) values at the centre of the beam for varying load signal amplitudes

The graph indicates that the base in-plane amplitude(X) of the TRS is increasing and more importantly the peaks at the locations of the holes are increasing in height relative to the base levels with the increment of load signal amplitude. For example, at 2kN load signal amplitude the base level of the TRS in-plane amplitude(X) is between  $0.2 \times 10^{-4}$  and  $0.4 \times 10^{-4}$ , while it is between  $1.2 \times 10^{-4}$  and  $1.4 \times 10^{-4}$  for 10kN load signal amplitude. Also, the peaks at 2kn load signal amplitude are more or less indistinguishable from the noise levels present in the TRS while the peaks at 10kn load signal amplitude are much more prominent and distinguishable from the noise as they show a much higher deviation from the base level compared to the noise. This graph also can be improved by plotting the mean in-plane amplitude(X) over the width of the beam along the length of the beam. Figure 13 illustrates the improved version of this graph with less noise.

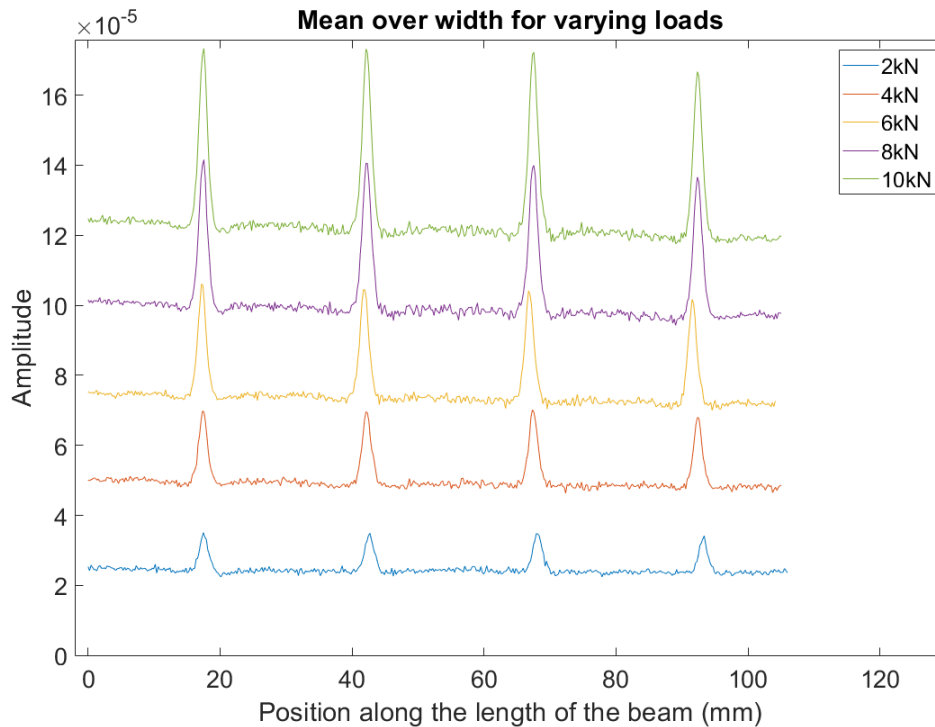


Figure 13 Mean in-plane amplitude(X) over the width of the beam along the length of the beam for varying load amplitudes.

#### 4.1.1.2. Effect of varying load frequencies (Uniaxial)

Similarly, to observe the effect of varying frequencies of the load signal on the TRS recorded by the microbolometer, the same specimen was tested at 2Hz, 4 Hz, 6 Hz, 8 Hz, and 10 Hz load signal frequencies at 15kN of mean and 10kN amplitude as specified in the methodology section. Figure 14 shows the TRS in-plane amplitude(X) values at the centre

of the beam plotted against the position along the length of the beam for each of the frequency in the same graph.

As illustrated by Figure 14, at 2Hz the results are not promising in terms of distinguishability of the location of the damages or the holes. The peaks at the holes are barely distinguishable from the noise and the base level of amplitude is quite low which is around  $0.85 \times 10^{-4}$  compared to the other frequencies that are around  $1.2 \times 10^{-4}$ . The gap between the TRS amplitudes of 2Hz test and 4Hz test is significantly larger than that of all other frequencies whose plots are indistinguishable from each other in this graph due to high levels of noise.

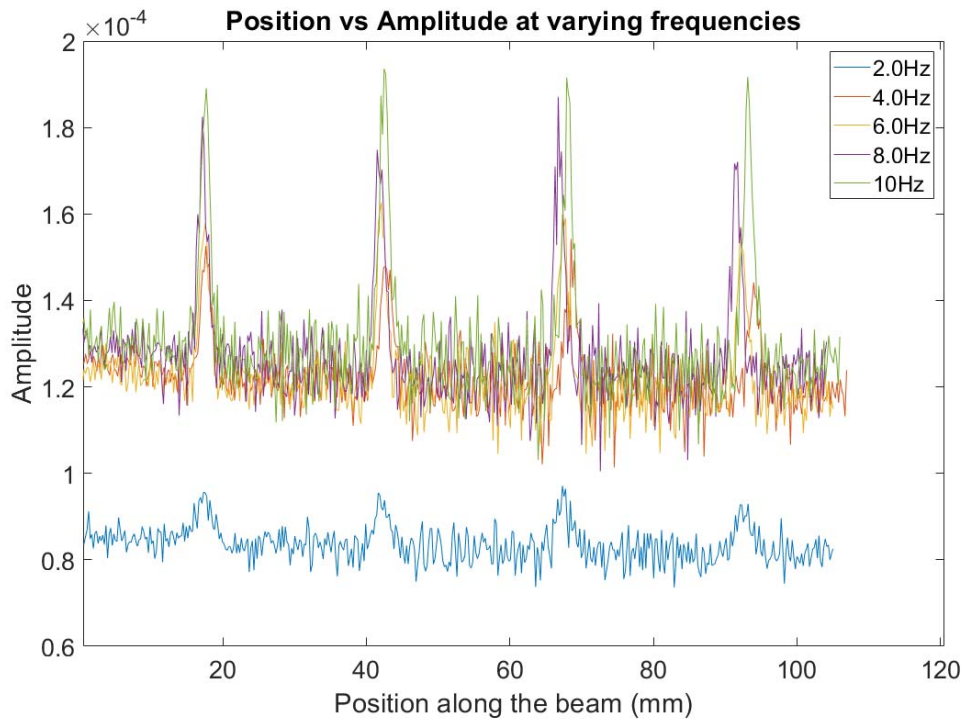


Figure 14 TRS in-plane amplitude(X) values at the centre of the beam for varying frequencies

Again, the noise in these plots can be reduced by calculating the mean in-plane amplitudes(X) over the width of the beam along the length of the beam which is illustrated in Figure 15. With this reduced noise levels, the plots for 4Hz to 10Hz now can be observed separate from each other. Unlike in the varying loads test the varying frequencies do not seem to have a linear effect on the TRS s generated.



The base amplitude levels for each frequency are at the sequence of 2Hz < 6Hz < 4Hz < 8Hz < 10Hz with are larger gap between 2Hz and 6Hz and much smaller gap between the others. However, interestingly the peak heights relative to the base level for each frequency are in the ascending order of the frequencies.

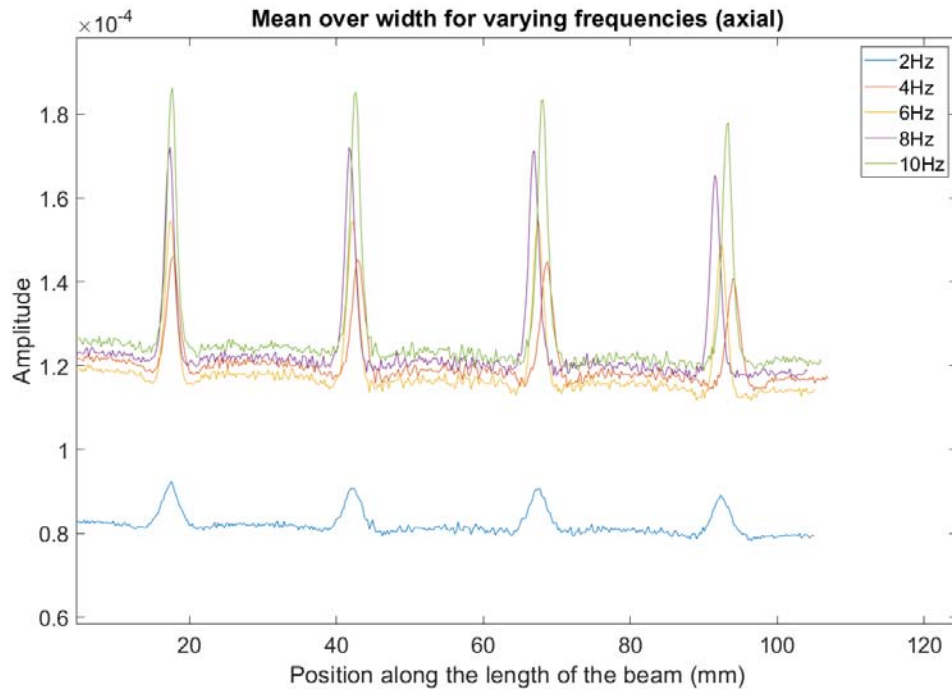


Figure 15 Mean in-plane amplitudes(X) over the width of the beam for varying frequencies.

#### 4.1.1.3. Effect of varying depths of damage (Uniaxial)

Also, to observe the effect of varying depths of the damage on the TRS recorded by the microbolometer, the four specimens with varying depths of holes' location at 1 mm, 1.5 mm, 2.5 mm, 3 mm, 3.5 mm, 4.5 mm, and 5 mm were tested with a load signal at 15kN of mean, 10kN amplitude and 6Hz of frequency as specified in the methodology section. Figure 16 shows the mean TRS in-plane amplitudes(X) over the width of the beam plotted against the position along the length of the beam for each of the depth in the same graph.



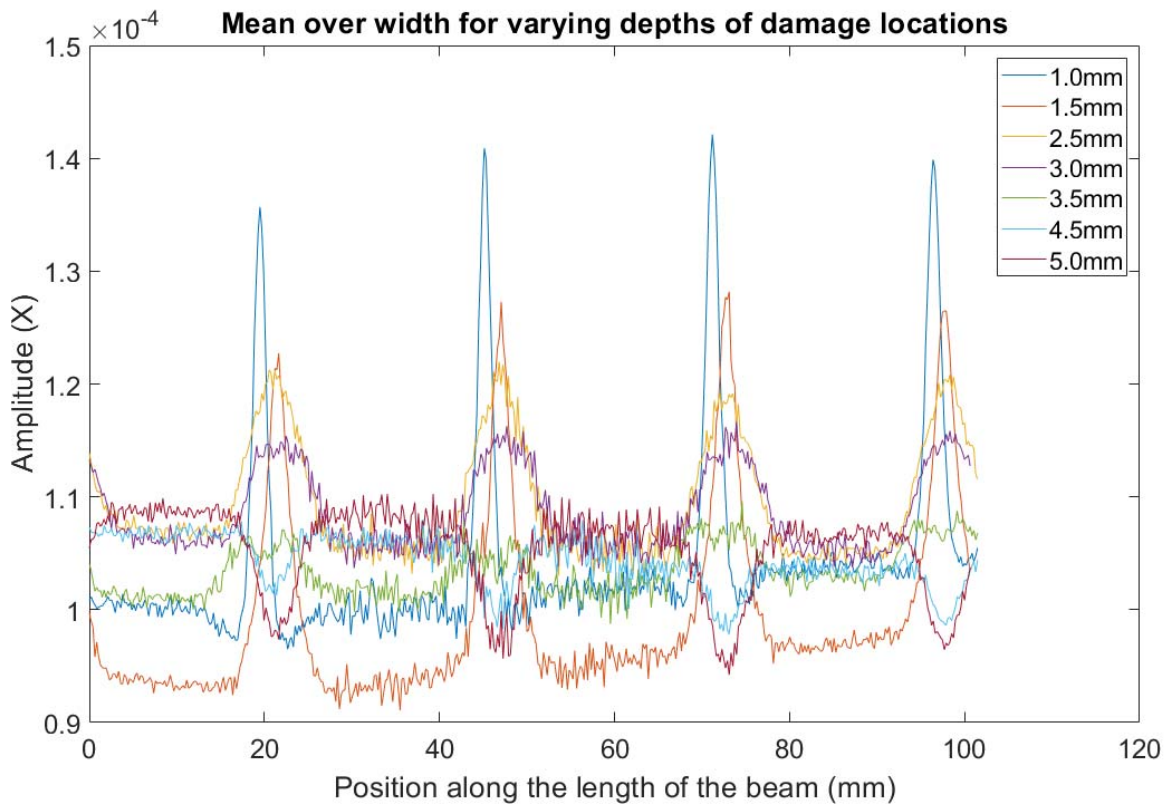


Figure 16 Mean TRS in-plane amplitudes(X) over the width of the beam for varying depths of defects.

The base level of each graph is at a different amplitude level which makes it harder to see the variations of the relative heights of peaks at the locations of holes. Therefore, each plot is calibrated to a similar base level by shifting each data set to have the same mean value in their Gaussian distribution equal to the mean value of the Gaussian distribution of the beam with holes at 1mm depth used for this test which is  $1.0308 \times 10^{-4}$ . This calibrated graph is illustrated in Figure 17.

Between 1mm depth to 3mm depth, the peak heights relative to the base levels are decreased and an interesting pattern emerges at depths larger than 3.5mm where the plots start to show troughs at the locations of the holes instead of peaks.

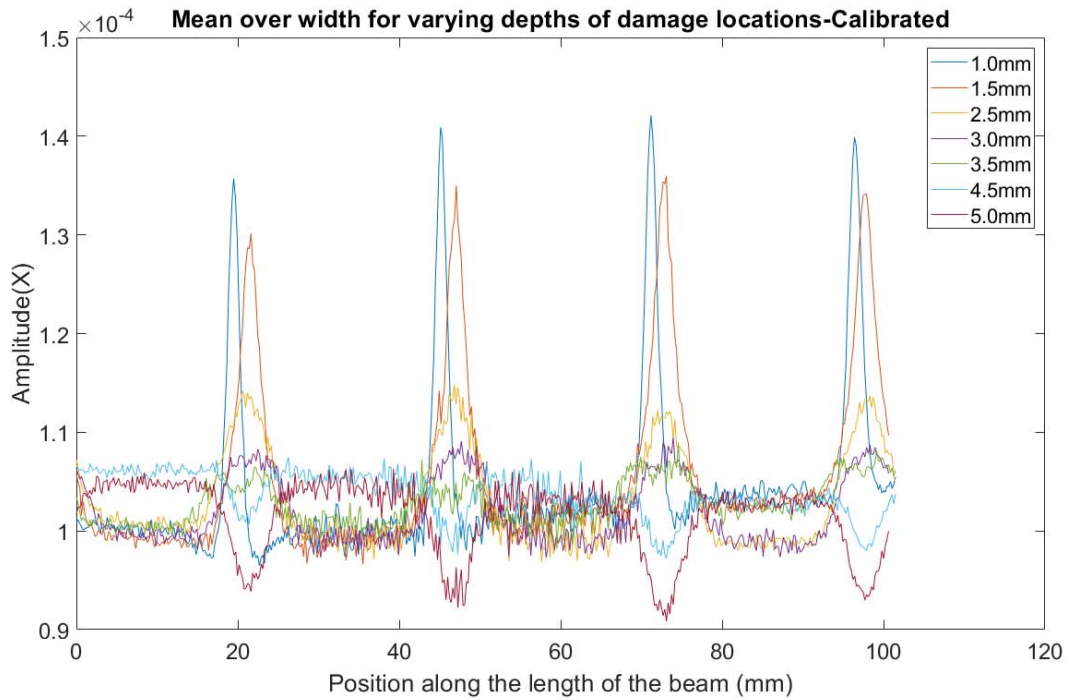


Figure 17 Calibrated mean TRS in-plane amplitudes(X) over the width of the beam for varying depths of defects.

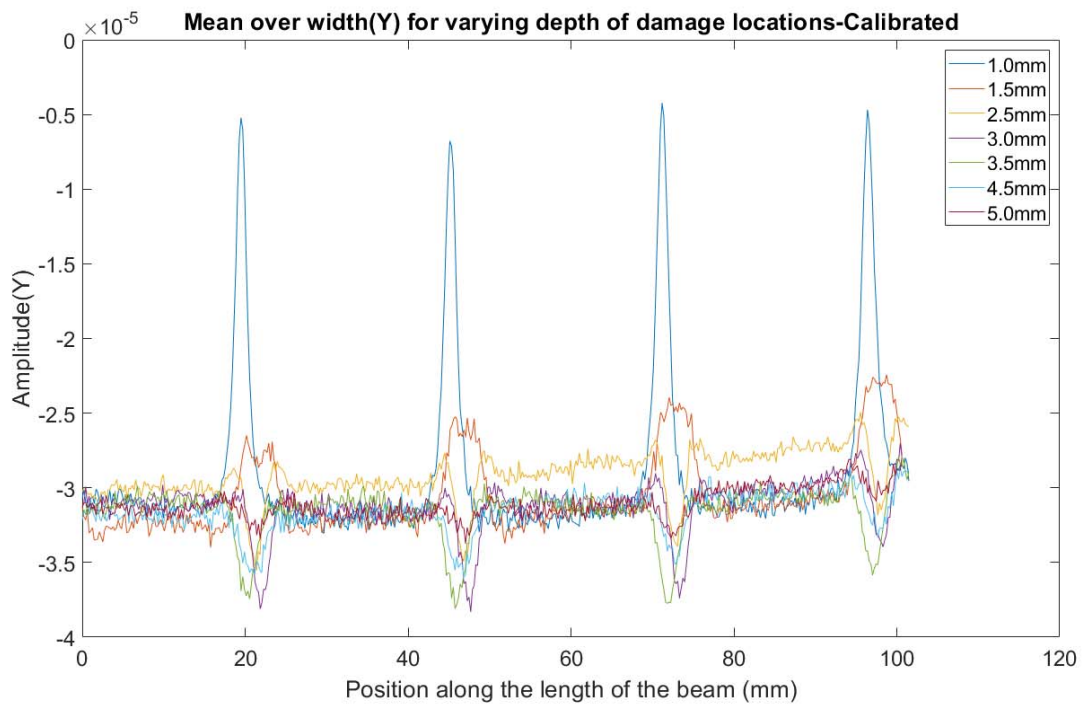


Figure 18 Calibrated mean TRS in-plane amplitudes(X) over the width of the beam for varying depths of defects.

A similarly calibrated plot was obtained for the quadrature amplitude(Y) measurements of the TRS which is shown in Figure 18. Here the peaks start to turn into troughs at 2.5mm depth which is lower than that of the in-plane graph. Also, the peaks and troughs seem to be less distributed compared to that of the in-plane graph upon visual inspection of the graph.

## 4.1.2. Flexural cyclic loading experiment

### 4.1.2.1. Effect of varying load amplitudes (Flexural)

The next test was the flexural loading case of the beam with holes at 1mm depth. First, the effect of the magnitude of the applied flexural load was tested by controlling the deflection of the beam at the point of applied load. Figure 19 shows the mean TRS in-plane amplitude(X) over the width of the beam along the length of the beam plotted against the position along the length of the beam for each of the displacement in the same graph.

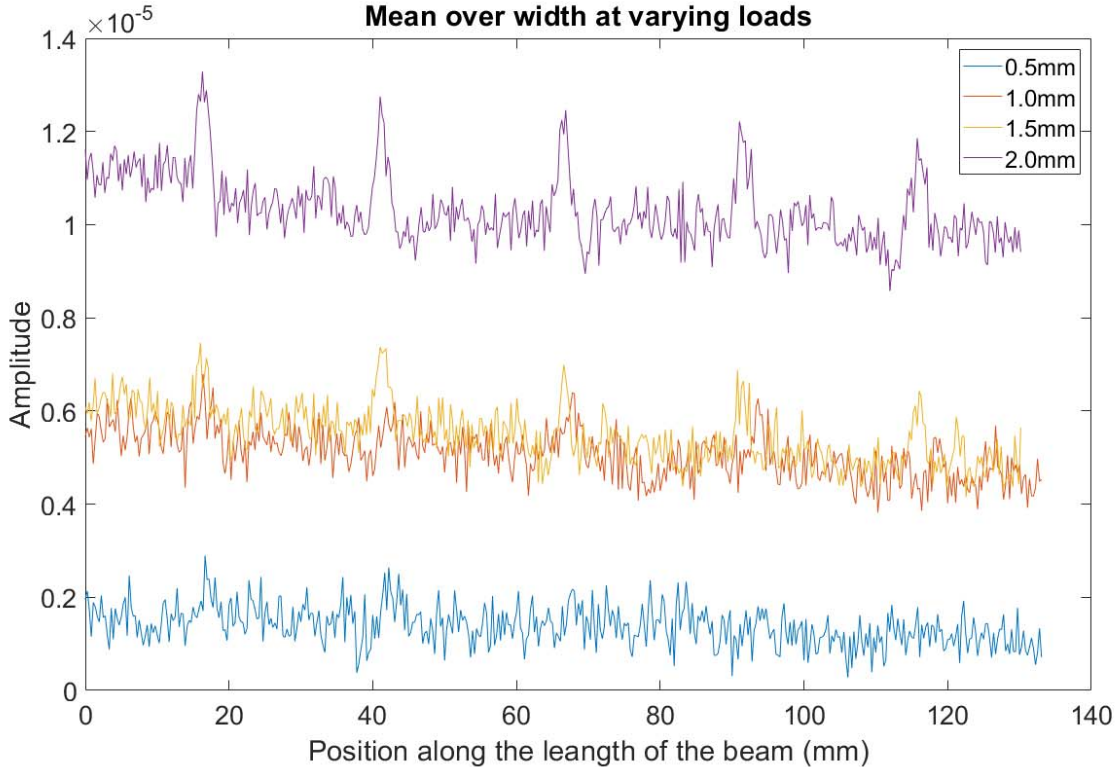


Figure 19 Mean TRS in-plane amplitude(X) over the width of the beam for varying loads.

Even though the graph for 2mm displacement has distinguishable peaks at the locations of the holes, none of the other displacements does not seem to show clearly distinguishable peaks from the noise present in them. Even the graph of 2mm displacement has high noise levels and low peak heights and the TRS in-plane amplitude(X) levels are overall much smaller than that of the axial loading test results. Even the highest amplitude(X) recorded is lower than  $0.14 \times 10^{-4}$  which is even lower than the lowest base level recorded for the varying axial loads test which is slightly above  $0.2 \times 10^{-4}$ . The amplitude(X) levels have still increased with the increased levels of displacement or the bending load. However, both the 1mm and 1.5mm displacements have resulted in almost the same level of amplitude(X).

#### 4.1.2.2. Effect of varying frequencies (Flexural)

Next, the effect of the frequency of the applied flexural load was tested. Figure 20 shows the mean TRS in-plane amplitude(X) over the width of the beam along the length of the beam plotted against the position along the length of the beam for each of the frequency tested in the same graph.

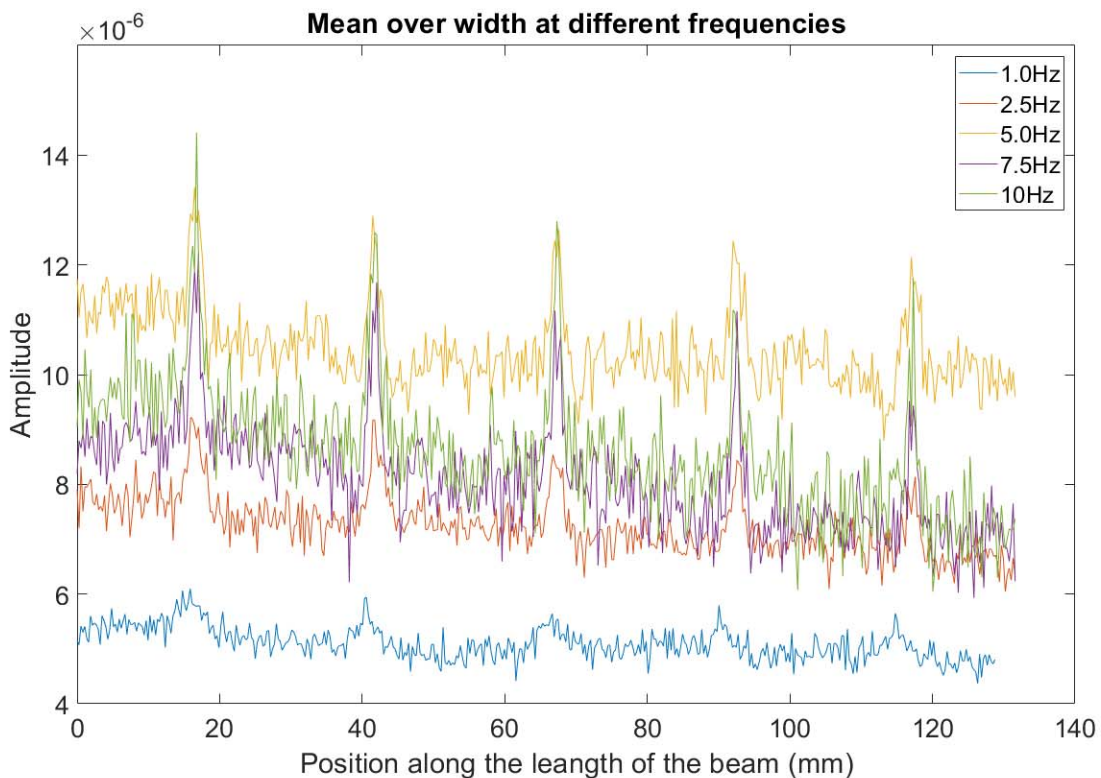


Figure 20 Mean TRS in-plane amplitude(X) over the width of the beam for varying frequencies.

Here an interesting observation can be made where 5Hz results in the highest base level of TRS in-plane amplitude(X) even though rest of the frequencies follow an increasing pattern of amplitudes(X) for increasing frequencies. However, it is evident that 10Hz resulted in tallest peaks relative to the base level at the locations of the holes.

## 4.2. FEA modelling

Finally, Ansys Workbench software was utilized for developing models for Finite Element Analysis (FEA) of the axial cyclic loading tests for comparing the simulated results with the real-world test data in order to evaluate the validity of the models. Figure 21 shows the temperature variation (mK) visualized in the FEA model at 6Hz.

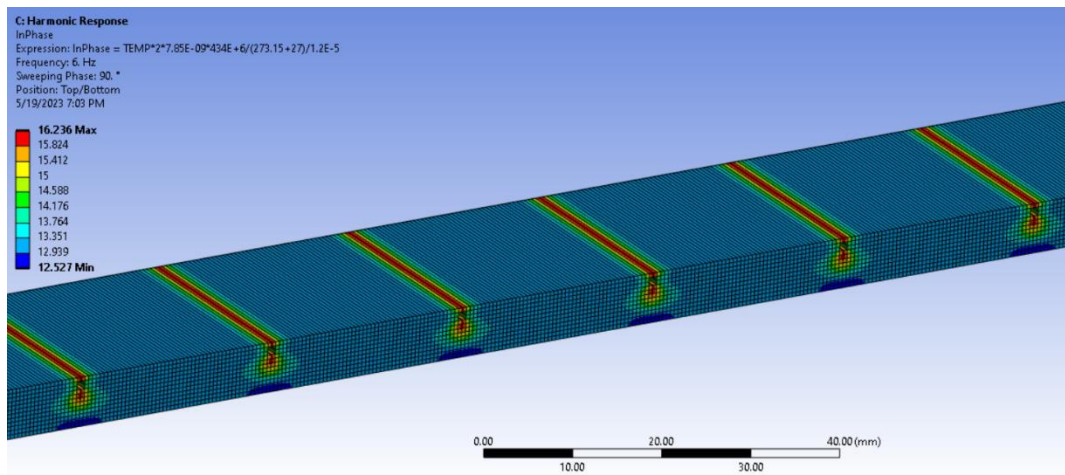


Figure 21 Temperature variation (mK) visualized in the FEA model at 6Hz

Figure 22 illustrates the in-plane temperature variation(mK) results of the FEA model for varying axial loads plotted against the position of the beam along the length. The results clearly resemble the same pattern of the actual varying axial loads test results shown in Figure 13 which is evidence for the validity of the FEA model.

Similarly, the effects of varying frequencies at 10kN load amplitude were modelled which is illustrated in Figure 23. However, this graph does not closely resemble the actual test results for varying frequencies shown in Figure 15. Here the base levels of the graphs do not vary much with the varying frequencies unlike the actual test results. Also, the peak heights relative to the base level show a proportional increment to the increasing frequencies which was not the case for the real-world test.



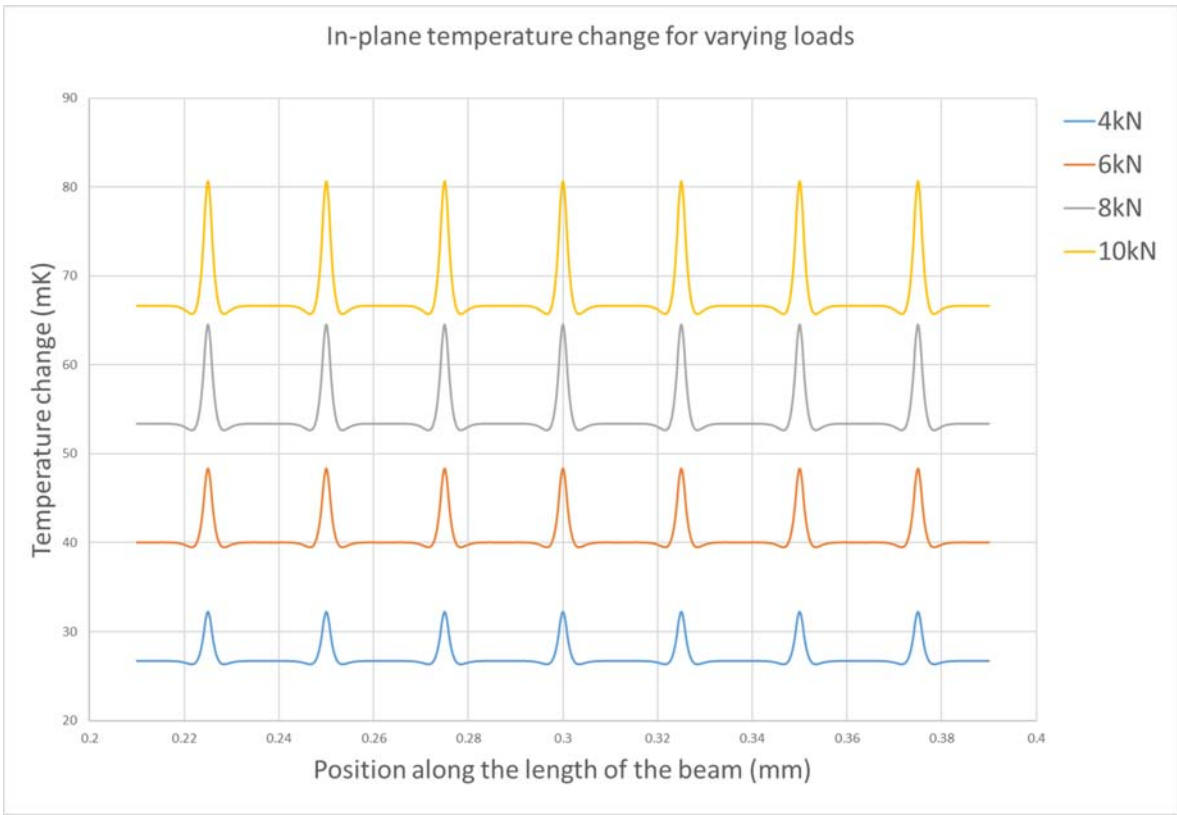


Figure 22 In-plane temperature variation(mK) results of the FEA model for varying axial loads

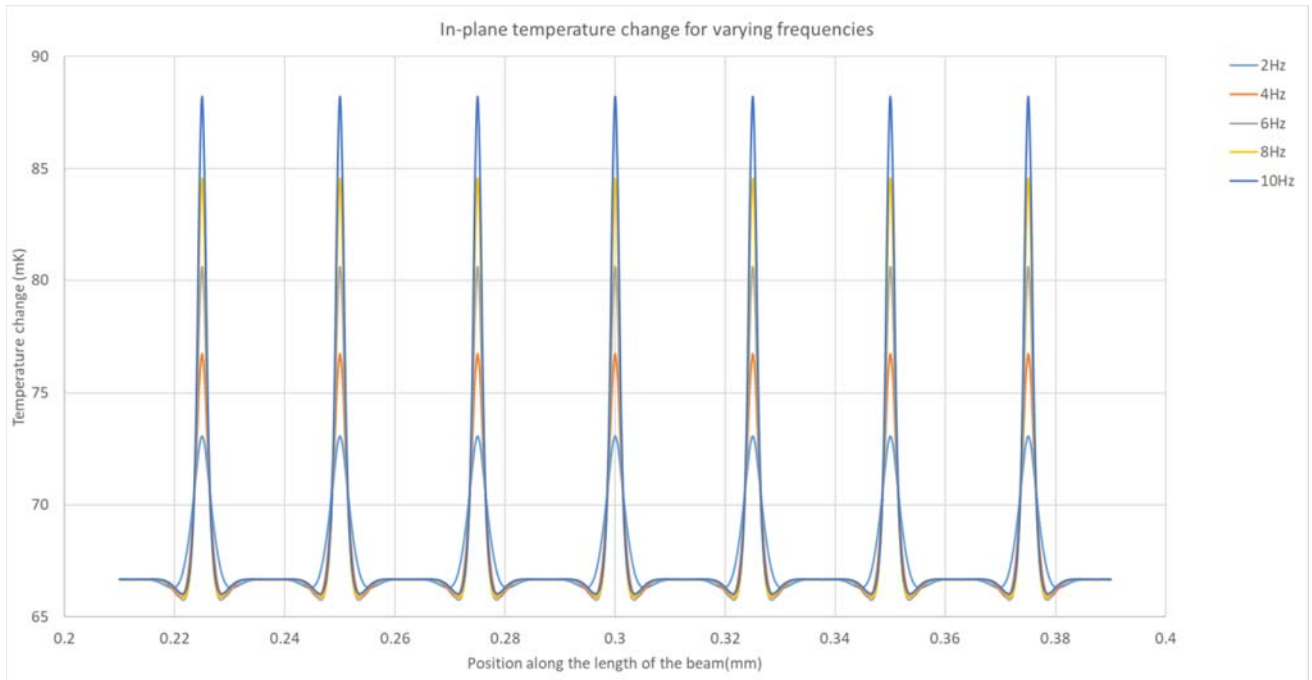


Figure 23 In-plane temperature variation(mK) results of the FEA model for varying frequencies.

## 5. DISCUSSION

As described by the thermoelastic effect, subjecting a material to cyclic loading generates temperature variations which in adiabatic conditions, the temperature change in isotropic materials correlates directly with the sum of the two principal stresses acting on the surface. Therefore, this temperature variation can be used for detecting the stress field on the surface of a loaded member using TSA technique. This stress field can be then analysed to identify stress concentrated locations which may indicate defects or damages in the loaded member. Most of the results are presented for the TRS in-plane amplitudes(X) recorded from the experiments as the peak amplitude of the stress sum at a specific point on the structure is directly related to the in-plane amplitude. The quadrature shows where heat diffusion is more significant, which happens in areas with high-stress gradients such as cracks or small defects (Rajic & Galea, 2015).

### 5.1. Varying load amplitudes (Uniaxial)

According to the results of the axial loading test carried out, there are stress concentration zones at each location of the drilled holes indicated by the peaks in the graph (Figure 13) even though they are internal defects. When the amplitude of the load signal is increased the TRS amplitude is also increased proportionally which is evident from the similar gaps between each plot with an increment of 2kN in the load signal. Also, the peak heights relative to the mean level of amplitude is increased. This is expected according to equation (1) as the principal stresses are increased with the increased load amplitude. Proportionally, the peak heights are increased which is caused by stress concentrations at the locations of holes.

Furthermore, the noise levels present in the TRS graph were reduced considerably using the mean over width method. Even though it reduced noise of the results in this experiment, this method may not produce accurate results for defects with smaller volume such as point defects as taking the mean amplitude value over the width does not represent such a small defect accurately. Therefore, plotting data of a line along the length of the specimen which is shown in Figure 12 illustrates a more accurate representation of data for such small defects. For this experiment, the mean amplitude over width plot is a fairly accurate representation of the stress distribution as the defects or the holes in the beam are present throughout the width of the beam with a constant cross section.

To understand the relationship between the stress present in the beam and the TRS amplitude, first the data was plotted in the form of a Gaussian distribution and the fitted Gaussian curve was determined using a MATLAB script. For example, following curves in Figure 24 show the Gaussian distributions and the fitted curves of in-plane and quadrature amplitudes of the axial loading test at 10kN load amplitude, 15kN mean and 6Hz of frequency.

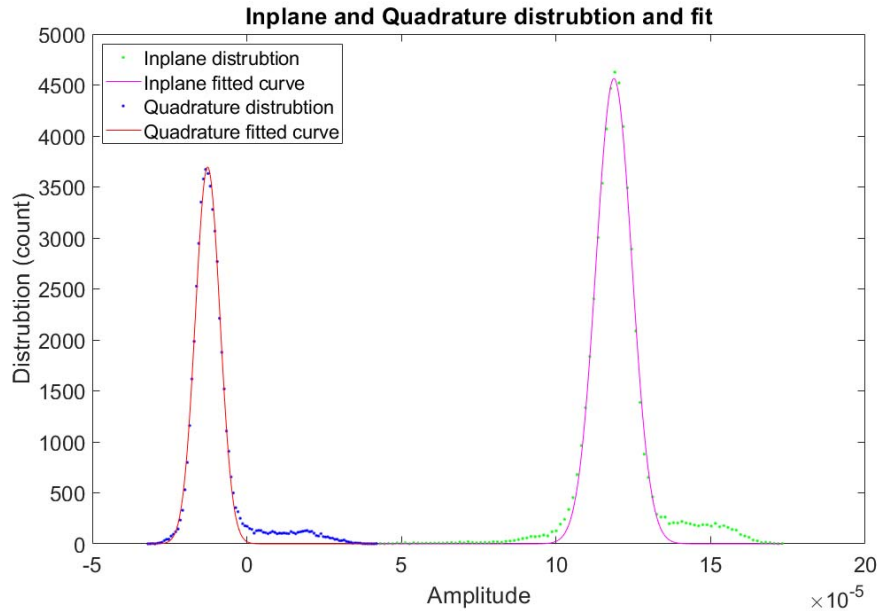


Figure 24 Gaussian fitted curves of in-plane and quadrature amplitudes of the axial loading test at 10kN load amplitude, 15kN mean and 6Hz of frequency.

The mean value of the fitted curve which is same as the mode value in a gaussian distribution represents the most repeated amplitude in the distribution. In other words, the mean value represents the TRS amplitude at the undamaged area of the beam which is the majority of the beam. Therefore, this mean value of the gaussian fitted curve reflects the stress distribution of an undamaged beam which can also be easily calculated using,

$$\sigma(stress) = F(Force)/A(Area)$$

This is helpful in developing a relationship between the stress present in the beam and the TRS amplitude by plotting the mean values of the gaussian distributions against the load



amplitudes as shown in Figure 25. Error bars for two standard deviations are illustrated in the plot which represents the noise levels at each load amplitude.

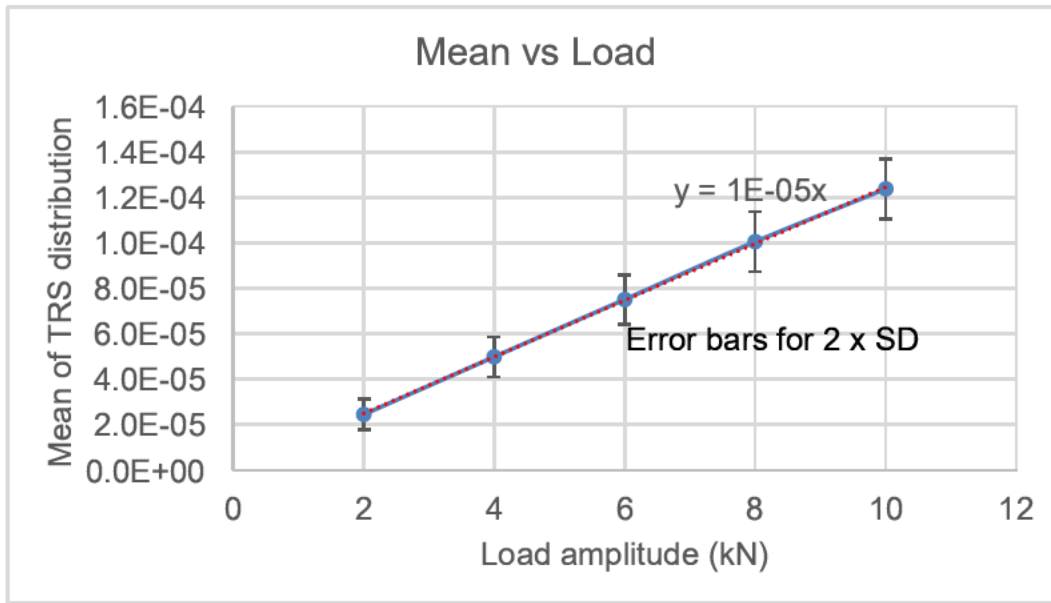


Figure 25 Mean values of the gaussian distributions against the load amplitudes.

A trendline was drawn to obtain the relationship between the X and Y values in the plot, which is represented by,

$$Y = 1 \times 10^{-5}X$$

This linear relationship represents the correlation of the TRS amplitude to the stress in the beam as shown below.

$$M = 1 \times 10^{-5}(F)$$

Since,

$$F(kN) = \sigma(kPa) \times A(m^2)$$

$$F = \sigma \times (150) \times 10^{-6}$$

Therefore,

$$M = 10^{-5}(\sigma \times (150) \times 10^{-6})$$

$$M = 150 \times 10^{-11}(\sigma)$$

$$\sigma(kPa) = \frac{M \times 10^{11}}{150} \quad (3)$$

Where,

$M$  = TRS in-plane amplitude,  $F$  = Load amplitude,  $\sigma$  = In-plane stress amplitude,  $A$  = Cross sectional area of beam

It is important to note that this relationship is only valid for the conditions set for this experiment and may change with variations of parameters such as the mean of the load signal which was set to 15kN during this experiment. A lower mean value or a higher amplitude of the load signal may introduce compressive forces to the beam which may cause changes to this relationship.

Another important factor to analyse is how much the peaks are distinguishable from the noise at different load amplitude levels. The graph in Figure 26 was plotted in order to analyse this in terms of peak heights and the standard deviations at each load amplitude.

Here, the plot marked with triangles illustrates the difference between the average of highest TRS in-plane amplitude values recorded at each load and the mean of the gaussian curve for that load, while the other curve illustrates the value of two standard deviations of the gaussian curve to include about 95% of the data which represents the noise levels accurately at each load amplitude. Therefore, the gap between these two graphs represents how much the peaks are above the noise levels and hence how well distinguished. According to the data represented in Figure 26, the distinguishability of the peaks increases with the load amplitude, hence the defects are more accurately detectable at higher load amplitudes.

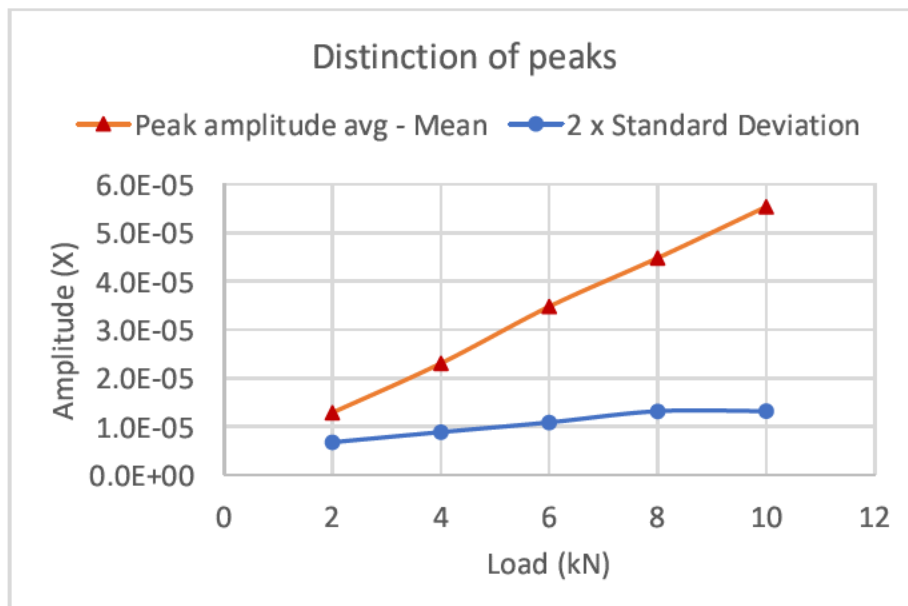


Figure 26 Noise level against the peak levels

## 5.2. Varying frequencies (Uniaxial)

Figure 15 illustrates the effect of frequency for the behaviour of the TRS recorded by the microbolometer. At 2Hz it demonstrates that the temperature variations captured are not reliable enough to detect the damages as the peaks are too low and almost indistinguishable from the noise. When the frequency is increased from 2Hz up to 4Hz the base level of TRS amplitude is increased by almost  $0.4 \times 10^{-4}$  of TRS amplitude. But from 4Hz to 6Hz of the load signal shows a slight decrease of the TRS base levels and again shows slight increase for 8Hz and 10Hz respectively. However, these gaps are much smaller than the gap between 2Hz and 4Hz and are almost negligible. This is illustrated in a graph in terms of the mean of TRS amplitudes distribution against the frequency in Figure 27 which indicates that the TRS output does not correlate to the load signal frequency in a proportional and linear manner unlike the load amplitude. The optimum frequency level for achieving the maximum TRS amplitude levels using TSA method may depend on the natural frequency of the member being tested. More research needs to be carried out in order to draw conclusive findings on the optimum level of frequency to achieve the maximum TRS amplitude level. However, similar graph to the graph in Figure 26 can be plotted for varying frequencies (Figure 28) to visualize how distinguishable the peaks are at each frequency level.

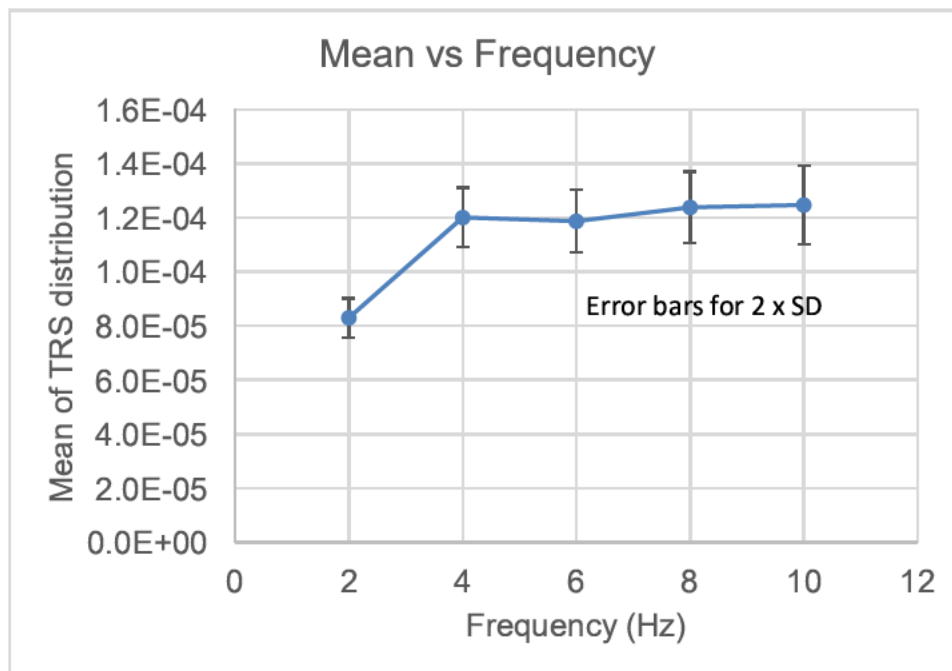


Figure 27 Mean values of the gaussian distributions against the frequencies.

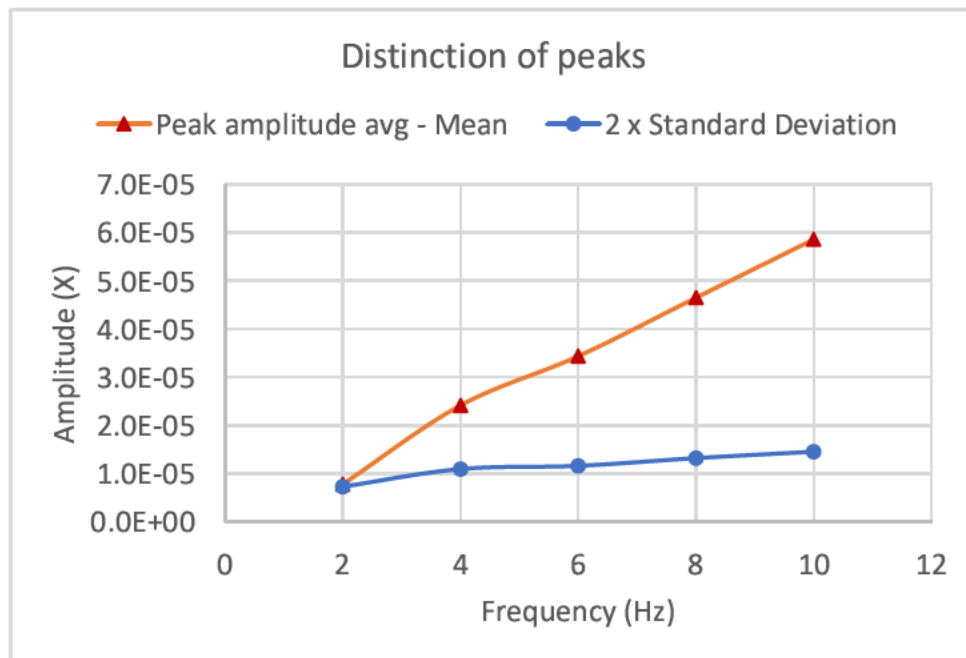


Figure 28 Noise level against the peak levels

These two graphs in Figure 28 validates that at 2Hz the peaks are almost indistinguishable while the peaks are more and more distinguishable when the frequency is increased. Furthermore, the graph marked with triangles indicates that the peak heights that is above the noise levels are almost linearly increased proportional to the frequency while the other graph which is also nearly linear indicates that the noise levels only slightly increase proportionally to the frequency. Therefore, it is evident that even though the mean TRS amplitude does not correlate to the frequency level in a linear manner, a higher frequency is desirable for detecting internal defects using TSA method.

### 5.3. Varying load amplitudes (Flexural)

Similarly, data can be analysed for the bending test by plotting the same graphs from the data collected for both varying displacements (loads) and varying frequencies experiments. However, as Figure 30 illustrates, the peaks are even below the noise levels indicating that the defects are not clearly distinguishable for any of the tested levels of flexural loads. The data recorded for the flexural loading test is one order of magnitude lower compared to the axial loading experiment's results. This can be overcome using a higher performing EMS that can exert much higher loads and displacements. Since the peak heights indicate an upward trend in Figure 30 whereas the noise levels have plateaued this trend suggests that the peak levels will be above the noise levels at higher displacements.

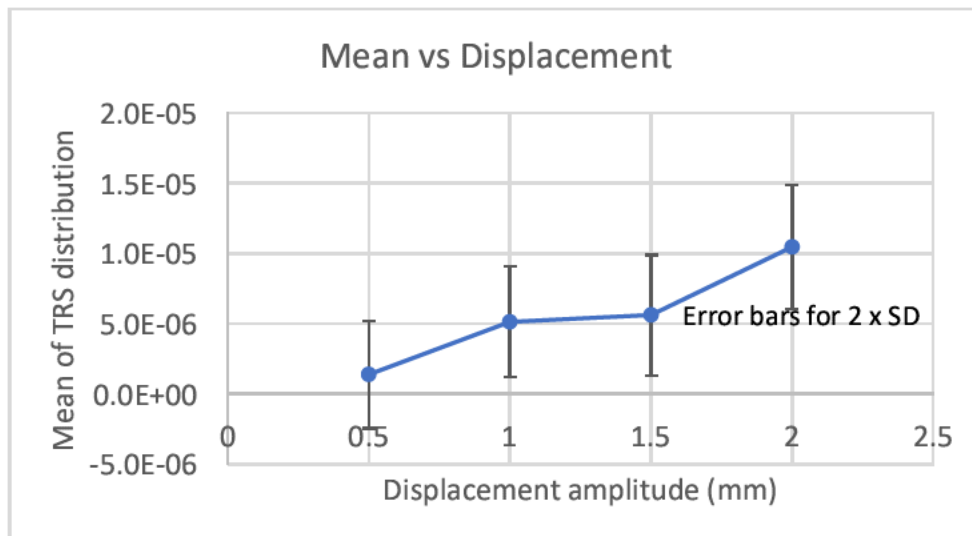


Figure 29 Mean values of the gaussian distributions against the displacement (loads)

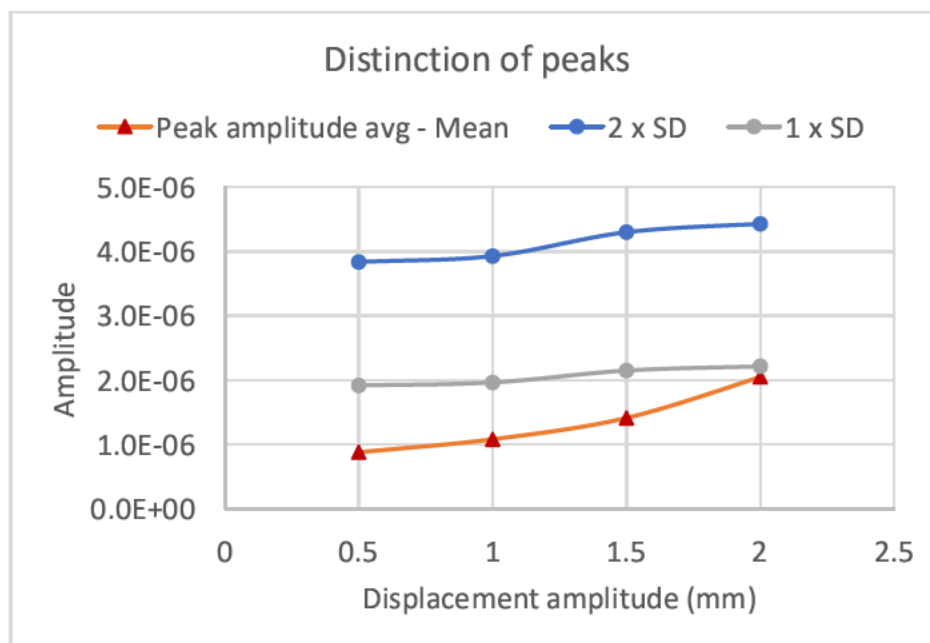


Figure 30 Noise level against the peak levels

#### 5.4. Varying frequencies (Flexural)

For varying frequencies of the flexural loading test at 2mm displacement, the graphs illustrate a similar behaviour to the varying displacements test as the peaks are not well distinguished at any of the frequencies which is evident from the peak heights plot being below the noise levels in Figure 32.

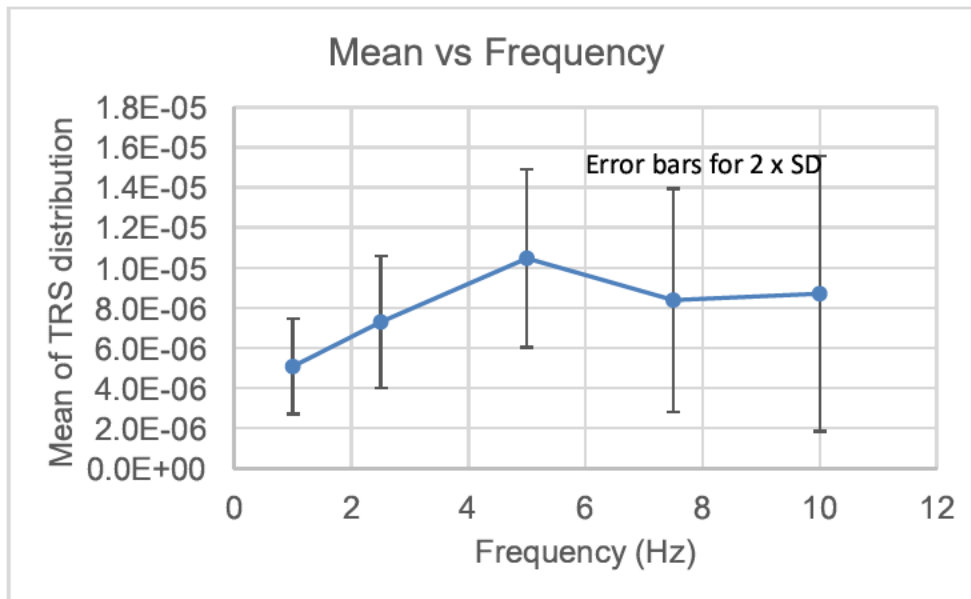


Figure 31 Mean values of the gaussian distributions against the frequencies.

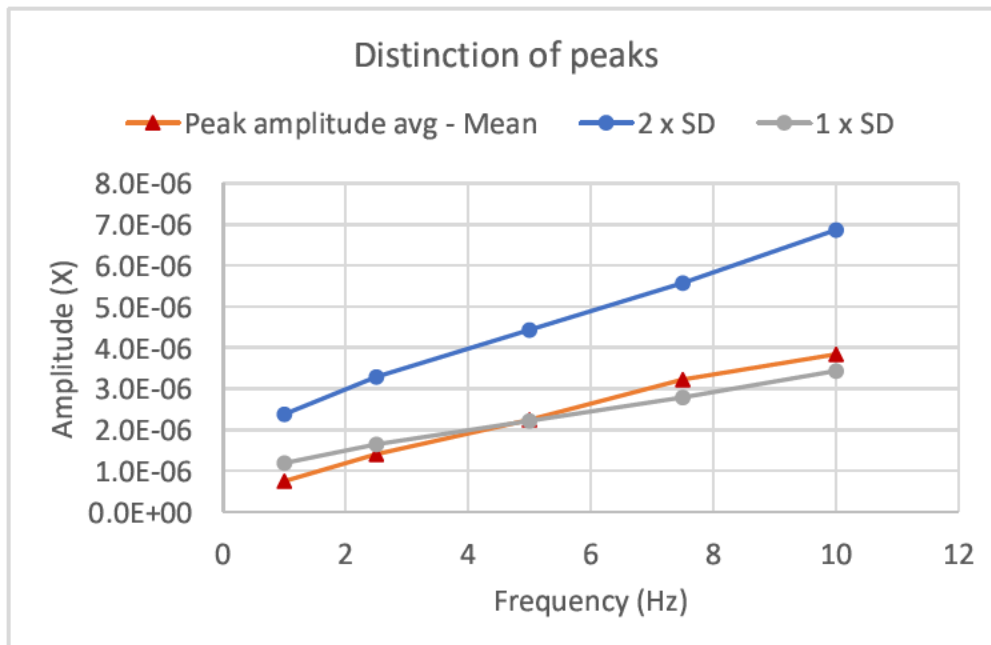


Figure 32 Noise level against the peak levels

The noise levels and the peak heights are increased with a slightly higher gradient for noise levels than that of the peak heights with increasing frequencies of the load signal. Therefore, it is unclear whether the peak heights will rise above the noise levels adequately at any load

signal frequency at this load amplitude. Therefore, further study has to be carried out at higher load amplitudes in order to determine an optimum frequency range for the beam.

### 5.5. Varying depths of damages (Uniaxial)

Furthermore, the results of the experiment in which varying depths of the holes from the observed surface of the beam was tested is analysed to evaluate the distinguishability of the peaks at the defect locations. However, in the graphs illustrated in Figure 33 and Figure 34 the absolute value of the difference between the peak average TRS amplitude and the mean was used as at some of the depths there are troughs instead of peaks in the graph in Figures 17 & 18. Taking the absolute value keeps the peak height a positive value which is helpful for evaluating the distinguishability of the peaks from noise.

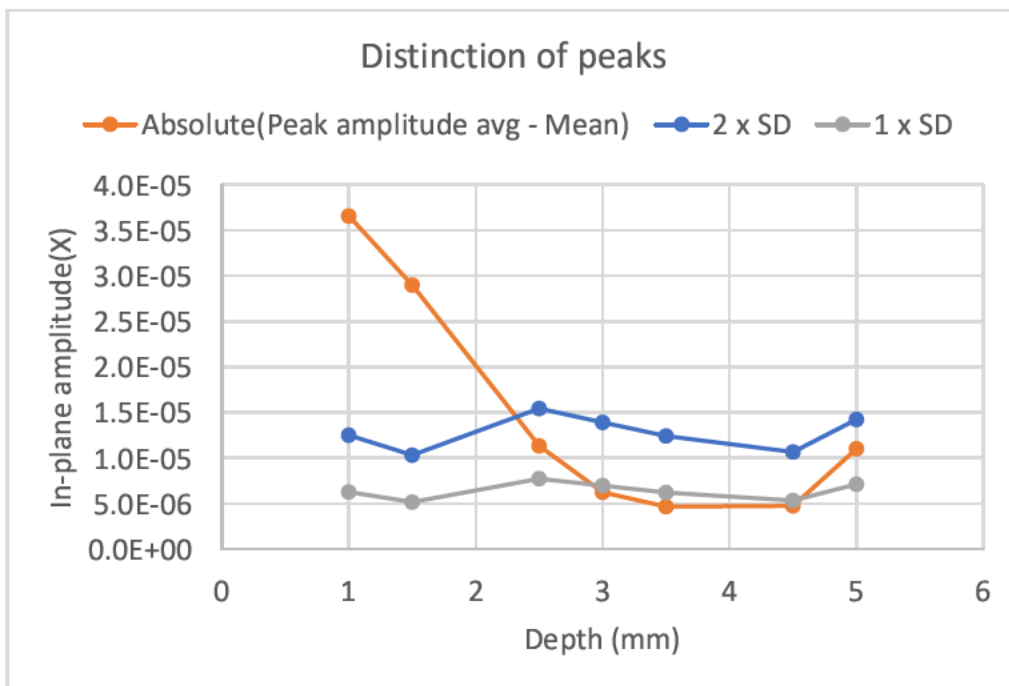


Figure 33 Noise level against the peak levels of in-plane amplitude(X) for varying depths

Figure 33 illustrates the TRS in-plane amplitude behaviour while Figure 34 illustrates the TRS quadrature amplitude behaviour. It is evident that both the 1mm and 1.5mm depths are higher above the noise levels in the in-plane amplitude plot (Figure 33) which is not the case for the quadrature amplitude plot (Figure 34) that shows the 1.5mm depth is below two standard deviations.

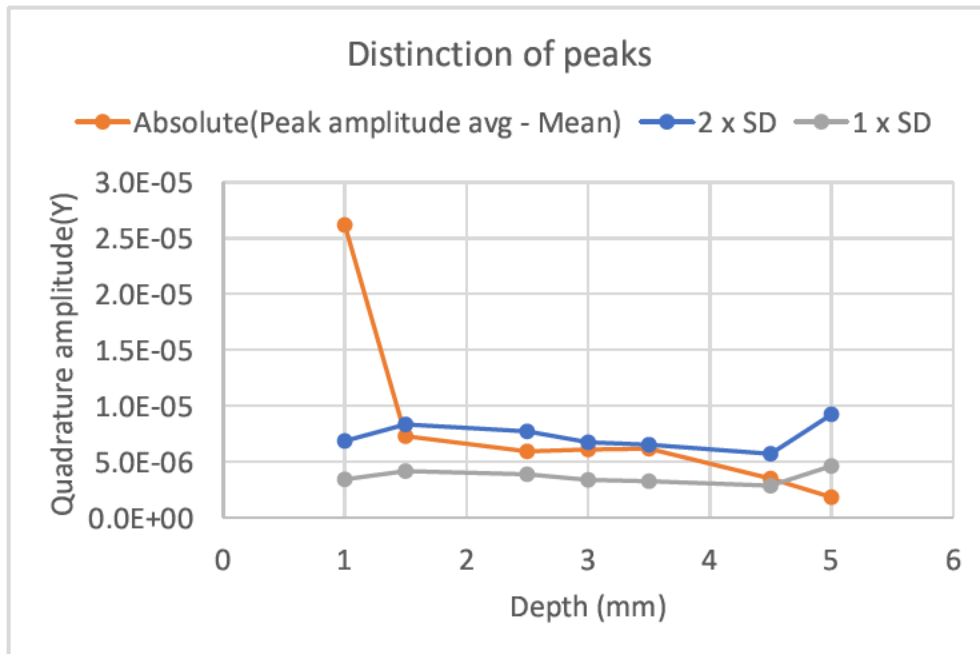


Figure 34 Noise level against the peak levels of quadrature amplitude(Y) for varying depths

However, majority of the data for depths between 2mm and 5mm are above one standard deviation in the quadrature amplitude plot which is not the case for the in-plane amplitude plot. Therefore, according to these two graphs it is evident that the quadrature amplitude data is superior for detecting the defects at higher depths of the beam whereas the in-plane data is superior for detecting the defects at lower depths.

## 5.6. FEA models

Finally, the FEA model shows an accurate representation of the real-world experimental data of the varying load case of the axial (tensile) loading experiment. However, the model simulating the varying frequency experiment does not accurately represent the findings of the real-world experiment which further indicates that more research needs to be done to verify the effects of frequency and the model needs to be further improved.

## 6. CONCLUSIONS

Analysis of the data from the uniaxial cyclic tensile loading experiment concludes that the TSA technique is an effective method for detecting and locating internal defects in metal structural members with high precision at sufficient loading amplitudes and desirable frequency levels. Evidently, higher load amplitudes improve the detectability of damages which can be utilized for detecting internal defects at higher depths from the observed outer



surface. The in-plane amplitude measurements are more capable of detecting internal damages closer to the surface whereas the quadrature amplitude measurements are more capable of detecting internal damages at higher depths from the observed outer surface.

Furthermore, while data suggests that higher frequency levels of the load signal improve the capability of detecting internal damages for TSA, the non-linear relationship of load signal frequency to the TRS amplitude levels needs to be further studied in order to draw conclusions. Another limitation of the research is that the flexural loading test did not produce conclusive evidence due to the limitations of the equipment used. However, statistical analysis of the experimental data suggests that TSA is capable of effectively detecting internal defects utilizing flexural loading at higher amplitudes. Finally, it is conclusive that the FEA model is highly accurate for the varying uniaxial loading case but does not accurately represent the varying frequency case further suggesting that more research needs to be done on the effects of varying frequency of the load signal. Overall, the study provides conclusive evidence to support that the TSA method is a highly capable full field NDT method for detecting internal defects in metals.

## **7. FUTURE WORK**

As discussed in both Discussion and Conclusion sections, more research needs to be carried out for building a superior understanding of the effects of varying frequency of the load signal on the damage detecting capabilities of the TSA method. Furthermore, the effectiveness of TSA method for flexural loading cases needs to be further studied at higher load amplitude levels to confirm the statistical data and draw conclusive evidence. Additionally, research into other parameters that may affect the capability of TSA method for detecting internal defects including the size or volume of the defect, material of the structural member under consideration and environmental conditions will assist in further establishing capabilities and limitations of the TSA technique for defect detection.

## 8. BIBLIOGRAPHY

Ancona, F., D. Palumbo, R. De Finis, G.P. Demelio, and U. Galietti. 'Automatic Procedure for Evaluating the Paris Law of Martensitic and Austenitic Stainless Steels by Means of Thermal Methods'. *Engineering Fracture Mechanics* 163 (September 2016): 206–19. <https://doi.org/10.1016/j.engfracmech.2016.06.016>.

De Finis, Rosa, Davide Palumbo, and Umberto Galietti. 'Evaluation of Damage in Composites by Using Thermoelastic Stress Analysis: A Promising Technique to Assess the Stiffness Degradation'. *Fatigue & Fracture of Engineering Materials & Structures* 43, no. 9 (September 2020): 2085–2100. <https://doi.org/10.1111/ffe.13285>.

Dulieu-Barton, J M, and P Stanley. 'Development and Applications of Thermoelastic Stress Analysis'. *The Journal of Strain Analysis for Engineering Design* 33, no. 2 (1 February 1998): 93–104. <https://doi.org/10.1243/0309324981512841>.

Dwivedi, Sandeep Kumar, Manish Vishwakarma, and Prof.Akhilesh Soni. 'Advances and Researches on Non Destructive Testing: A Review'. *Materials Today: Proceedings* 5, no. 2 (2018): 3690–98. <https://doi.org/10.1016/j.matpr.2017.11.620>.

Gdoutos, Emmanuel E. 'Thermoelastic Stress Analysis (TSA)'. In *Experimental Mechanics*, by Emmanuel E. Gdoutos, 261–67. *Solid Mechanics and Its Applications*. Cham: Springer International Publishing, 2022. [https://doi.org/10.1007/978-3-030-89466-5\\_13](https://doi.org/10.1007/978-3-030-89466-5_13).

Gdutos, Emmanuël. *Experimental Mechanics: An Introduction*. *Solid Mechanics and Its Applications*, volume 269. Cham: Springer, 2022.

Greene, Richard J., Eann A. Patterson, and Robert E. Rowlands. 'Thermoelastic Stress Analysis'. In *Springer Handbook of Experimental Solid Mechanics*, edited by William N. Sharpe, 743–68. *Springer Handbooks*. Boston, MA: Springer US, 2008. [https://doi.org/10.1007/978-0-387-30877-7\\_26](https://doi.org/10.1007/978-0-387-30877-7_26).

Hwang, Soonkyu, Yun-Kyu An, Ji-Min Kim, and Hoon Sohn. 'Monitoring and Instantaneous Evaluation of Fatigue Crack Using Integrated Passive and Active Laser Thermography'. *Optics and Lasers in Engineering* 119 (August 2019): 9–17. <https://doi.org/10.1016/j.optlaseng.2019.02.001>.

Takei, Ayad, J.A. Epaarachchi, Mainul Islam, J. Leng, and N. Rajic. 'Detection and Characterisation of Delamination Damage Propagation in Woven Glass Fibre Reinforced Polymer Composite Using Thermoelastic Response Mapping'. *Composite Structures* 153 (October 2016): 442–50. <https://doi.org/10.1016/j.compstruct.2016.06.044>.

Krstulovic-Opara, Lovre, Branko Klarin, Pedro Neves, and Zeljko Domazet. 'Thermal Imaging and Thermoelastic Stress Analysis of Impact Damage of Composite Materials'. *Engineering Failure Analysis* 18, no. 2 (March 2011): 713–19. <https://doi.org/10.1016/j.engfailanal.2010.11.010>.

Middleton, C. A., M. Weihrauch, W. J. R. Christian, R. J. Greene, and E. A. Patterson. 'Detection and Tracking of Cracks Based on Thermoelastic Stress Analysis'. *Royal Society Open Science* 7, no. 12 (December 2020): 200823. <https://doi.org/10.1098/rsos.200823>.

Mukhopadhyay, C. K., and Ravibabu Mulaveesala, eds. *Advances in Non-Destructive Evaluation: Proceedings of NDE 2019. Lecture Notes in Mechanical Engineering*. Singapore: Springer Singapore, 2021. <https://doi.org/10.1007/978-981-16-0186-6>.

Raj, B. 'Nondestructive Testing and Evaluation: Overview'. In *Encyclopedia of Materials: Science and Technology*, 6177–84. Elsevier, 2001. <https://doi.org/10.1016/B0-08-043152-6/01097-4>.

Rajic, Nik, and Chris Brooks. 'Automated Crack Detection and Crack Growth Rate Measurement Using Thermoelasticity'. *Procedia Engineering* 188 (2017): 463–70. <https://doi.org/10.1016/j.proeng.2017.04.509>.

Rajic, Nik, and Steve Galea. 'Thermoelastic Stress Analysis and Structural Health Monitoring: An Emerging Nexus'. *Structural Health Monitoring* 14, no. 1 (January 2015): 57–72. <https://doi.org/10.1177/1475921714548936>.

Rucka, Magdalena. 'Special Issue: "Non-Destructive Testing of Structures"'. *Materials* 13, no. 21 (6 November 2020): 4996. <https://doi.org/10.3390/ma13214996>.

Sathon, N., and Janice M. Dulieu-Barton. 'Damage Analysis of Internal Surface Flaws Using Thermoelastic Stress Analysis'. *Key Engineering Materials* 293–294 (September 2005): 279–88. <https://doi.org/10.4028/www.scientific.net/KEM.293-294.279>.

Sause, Markus G. R., and Elena Jasiūnienė, eds. *Structural Health Monitoring Damage Detection Systems for Aerospace*. Springer Aerospace Technology. Cham: Springer International Publishing, 2021. <https://doi.org/10.1007/978-3-030-72192-3>.

Wildy, Stuart J, Aaron J H Baker, John D Codrington, and Peter R Cook. 'Use of SLDV and FBG for the Detection of Delamination in Composite Laminate Beams: A Comparative Study', 2021.

Wong, A.K., J.G. Sparrow, and S.A. Dunn. 'On the Revised Theory of the Thermoelastic Effect'. *Journal of Physics and Chemistry of Solids* 49, no. 4 (January 1988): 395–400. [https://doi.org/10.1016/0022-3697\(88\)90099-6](https://doi.org/10.1016/0022-3697(88)90099-6).

# APPENDIX A

Figure removed due to copyright restriction.

Figure removed due to copyright restriction.

Figure removed due to copyright restriction.

Figure removed due to copyright restriction.



Figure removed due to copyright restriction.

Figure removed due to copyright restriction.

Figure removed due to copyright restriction.

Figure removed due to copyright restriction.

Figure removed due to copyright restriction.

Figure removed due to copyright restriction.

Figure removed due to copyright restriction.

Figure removed due to copyright restriction.



Figure removed due to copyright restriction.

Figure removed due to copyright restriction.

Figure removed due to copyright restriction.

Figure removed due to copyright restriction.

Figure removed due to copyright restriction.

Figure removed due to copyright restriction.

Figure removed due to copyright restriction.